What controls the formation of vulcanian bombs? A case study from the 1 February 2014 eruption of Tungurahua (Ecuador)

Alessia Falasconi, Raffaello Cioni, Benjamin Bernard, Pablo Samaniego, Marco Pistolesi, Federica Schiavi

What controls the formation of vulcanian bombs?

A case study from the 1 February 2014 eruption of Tungurahua (Ecuador)

*Alessia Falasconi[A] alessia.falasconi@unifi.it, Raffaello Cioni[A], raffaello.cioni@unifi.it, Benjamin Bernard[B], bbernard@igepn.edu.ec, Pablo Samaniego[C], pablo.samaniego@ird.fr, Marco Pistolesi[D], pablo.samaniego@ird.fr, Federica Schiavi[C], federica.schiavi@uca.fr

[A] Dipartimento di Scienze della Terra, Università di Firenze, Via G. La Pira, 4, 50121, Firenze, Italy

[B] Instituto Geofísico, Escuela Politécnica Nacional, Av. Ladrón de Guevara E11-253, Quito 170525, Ecuador

[C] Laboratoire Magmas et Volcans, IRD-CNRS-OPGC, Université Clermont Auvergne, 6 Av. Blaise Pascal, 63170 Aubière, France

[D] Dipartimento di Scienze della Terra, Università di Pisa, via Santa Maria, 53, 56126 Pisa PI

*corresponding author

Abstract

Vulcanian eruptions are very common at many volcanoes around the world that erupt intermediate to silicic magmas. This type of eruption generates a wide variability of bombs and blocks preserving information onto the conduit processes that strongly control the dynamics of these events. After 84 years of repose, a new cycle of eruptive activity of Tungurahua volcano (Ecuador) started in October 1999, consisting of recurrent low-to-moderate explosive phases, which included sporadic stronger Strombolian to sub-Plinian pulses, as well as Vulcanian outbursts. The 1 February 2014 eruption was one of the most important Vulcanian events and was characterized by highly energetic explosions resulting from a plug conduit failure that generated a ~9 km-high eruptive column and fallback pyroclastic density currents. Four different types of blocks and bombs were found in the deposits of the pyroclastic density currents: dense fragments (DB), breadcrust bombs (BCB), cauliflower bombs (CFB) and foliated, banded bombs (FB). All the different types of bombs have homogenous andesitic bulk-rock compositions but different, highly evolved matrix glass compositions ranging from rhyolitic for BCB to dacitic for CFB and DB, suggesting the occurrence of contrasting shallow crystallization processes within the conduit. The wide variability of the bombs in terms of patterns of surface cracks, external morphologies,

internal density and vesicularity gradients records different conditions of formation from a same magma composition.

The combination of morphological measurements, compositional data and textural analysis allow us (i) to infer the pre-eruption physical and rheological state of the conduit plug, (ii) to reconstruct the short-scale lateral and vertical gradients characterizing the plug, and (iii) to clarify the specific mechanism controlling the formation conditions of CFB, still poorly defined in the literature.

Keywords

vulcanian eruption; breadcrust bombs; cauliflower bombs; Tungurahua volcano

1. Introduction

Vulcanian explosions are small to moderate volcanic outbursts lasting seconds to minutes, which commonly originate from andesitic to dacitic magmas (Morrissey and Mastin, 2000). They form not-sustained plumes that are generally injected to tropospheric heights and dense showers of ballistic ejecta that are dispersed all around the vents. These eruptions are generally associated to sudden explosions of viscous magma during lava dome or plug formation (e.g., Sparks, 1997; Druitt et al., 2002; Cashman et al., 2008) and may occur as precursory phases of sub-Plinian or Plinian eruptions (Hammer et al, 1999; Cioni et al., 2015). This type of explosive activity has been related to the brittle failure of a rigid, hot plug of (partially) solidified magma, induced by the overpressure generated by progressive gas accumulation below or within the plug (Self et al., 1979; Woods, 1995; Morrissey and Mastin, 2000). Explosive eruptions of this type may generate different types of volcanic phenomena including pyroclastic density currents (PDCs) together with variably dispersed, thin ash fallout sheets. The ubiquitous presence of different types of large fragments (bombs or blocks) of juvenile material associated to the deposits of proximal ballistic showers or transported within PDCs represents one of the most typical features of Vulcanian deposits. Due to the coarse nature, the morphological, compositional and textural features of Vulcanian bombs record the pre- and syn-eruptive processes associated to this type of eruptions. Walker (1969, 1982) initially defined three different types of bombs: i) dense blocks that were hot upon impact but did not expand afterwards, ii) bombs with thick quenched rinds and limited expansion, and iii) highly expanded bombs. The term “breadcrust” has been typically used to describe the external morphology of the last two types of bombs.

Breadcrust bombs are generally characterized by dense, thick rinds and vesicular interiors and have multiple sets of surface cracks. They have been interpreted to result either from the rapid cooling, due to forced air convection during flight in the atmosphere, of a partially (pre-eruptively) degassed, high viscosity, silicic magma (e.g., Turcotte et al., 1990; Hoblitt and Harmon, 1993), or from the rapid quenching following interaction with external water (e.g., Fisher and Schmincke,1984). Wright et al. (2007) analysed the bombs related to the 1999 eruption at Guagua Pichincha volcano (Ecuador) and characterized from a textural point of view all these three types of bombs Based also on the measured volatile content still dissolved in the glass of the different types of bombs, Wright et al. (2007) discussed the observed textural differences between the bombs in terms of compositional and rheological vertical gradients in the magma occupying the conduit at the moment of the eruption. Colombier et al. (2022) and Wright et al. (2023) explore compositions, magma crystallinity and related texture of those breadcrust bombs in order to get more insights on decompression, degassing and magma ascent during the 1999-2001 eruptions at Guagua-Pichincha volcano.

Apart from breadcrust bombs, another important bomb category, known as “cauliflower bombs”, has been described in the literature. These are characterised by ellipsoidal shapes and present bulbous surfaces with microfractured, often microvesicular, thin rinds. In general, these were associated with more mafic magma compositions than those classically characterising breadcrust bombs and were generally described as ejecta in maars (Lorenz, 1973) or, more commonly, in dense PDC deposits (Nairn and Self, 1978; Alvarado and Soto, 2002; Cole et al., 2005; Miyabuchi et al., 2006). In addition, most of the authors in the literature associate cauliflower bombs (and in many cases also breadcrust bombs) to hydromagmatic processes (Lorenz, 1987; Heiken, 2006; Rosseel et al., 2006; Németh and Cronin, 2008; Martí et al., 2011; Fisher and Schmincke,1984; Németh and Kosik, 2020). Despite the suggestion that cauliflower bombs can be associated to mafic magma compositions, these are often observed to coexist with breadcrust bombs in the same deposits, so reflecting different conditions of formation from a same magma composition that have not yet been investigated in detail. Benage et al. (2014) numerically modelled the textural evolution of coarse pyroclasts during different transport and cooling regimes (buoyant plume vs. PDC) to explain the variable textures observed on bombs from eruptions of intermediate intensity and different composition. Based on their observations on PDC deposits at Tungurahua volcano (Ecuador), they suggested that cauliflower bombs are possibly related to cooling (and mechanical modifications) during PDC transport, while breadcrust textures mainly develop under

higher cooling rates typically associated to atmospheric ballistic trajectories. Benage et al. (2014) also estimated the possible maximum thickness of the external quenched rind of the bomb in few millimetres, similarly to what obtained by Wright et al. (2007).

With the purpose of understanding the pre-eruptive physical state of the magma and to derive a possible model of formation of dense blocks, breadcrust and cauliflower bombs ejected during the Vulcanian event occurred on February 1, 2014, at Tungurahua volcano, we describe here the physical features (e.g., density, surface cracks), textures and chemical compositions from a representative set of bombs, discussing their possible mechanisms of formation relative to the observed eruption dynamics.

2. Geological background and eruption chronology

Tungurahua volcano (Lat. 01°28'S; Long. 78°27'W) is located in central Ecuador (Fig. 1A), about 120 km south of Quito and 33 km southeast of Ambato, the capital of Tungurahua province. It is a steep-sided stratovolcano with an elevation of 5023 m above sea level; it is notable for the high relief (3200 m over the basement) and the presence of a small summit glacier (Hall et al., 1999; Bablon et al., 2018). Tungurahua is one of Ecuador's most active volcanoes and belongs to the main volcanic arc of the Ecuadorian Andes, along with other large edifices such as Sangay, Cotopaxi, Antisana, Cayambe and El Reventador (Hall et al., 1999). After 84 years of repose, a new eruptive period started in October 1999 with semi-persistent explosive activity of uneven intensity and style, which lasted until 2010. PDCs activity only began in July-August 2006 (Kelfoun et al., 2009; Douillet et al., 2013; Hall et al., 2013; Bernard et al., 2014) and was associated to some of the largest events. Starting from August 2013 a strong inflation was recorded from station RETU, located at 3950 m of elevation on the northern flank of the volcano, 2000 m north, and 1000 m below the summit vent (Neuberg et al., 2018). Inflation generally peaked shortly before each larger event, rapidly dropping days to hours before the eruption started, often in coincidence with the onset of large seismic activity (Neuberg et al., 2018).

One of the most important Vulcanian episodes started on February 1, 2014, after 77 days of weak background degassing and only 2 days of pre-eruptive seismic activity (Hall et al., 2015; Romero et al., 2017). After few sporadic explosions producing tephra fallout and a peak in seismicity on 30 January (Instituto Geofisico, 2014a), seismic activity decreased until 1 February when, between 01:10 and 20:30 UTC, a swarm of volcano-tectonic and long-period events was recorded from the monitoring network of the Instituto Geofísico and the Observatorio del Volcán Tungurahua (OVT;

http://www.igepn.edu.ec). The main eruption started at 22:12 UTC, following the abrupt failure of a conduit plug and resulting in a large explosion which formed a 5 km-high plume. This was rapidly followed by a phase of collapsing fountain that generated small- to medium-sized PDCs dispersed along the NW drainages of the volcano (Instituto Geofísico, 2014b; Hall et al., 2015). A similar PDCs distribution was generated by a new outburst occurred at 22:32 UTC. A third explosion, at 22:39 UTC, coincided with the paroxysmal Vulcanian phase of the eruption. This last explosion produced a sustained plume which lasted 9 minutes, reaching a height of 13.7 km asl (http://www.ssd.noaa.gov/VAAC/messages.html) and generating large PDCs (Instituto Geofísico, 2014c) that descended along at least nine ravines on the N, W and SW flanks down to the base of the edifice. The PDCs reached a maximum runout of ~ 8 km, velocities between 9.5 and 36 m s^{-1} (Hall et al., 2015), and transported a large amount of variably vesicular bombs and blocks. A final eruptive phase started at 23:36 UTC, characterized by Strombolian activity with discrete ejections of incandescent bombs and with frequent, low-altitude ash emissions. This activity continued for several days (Instituto Geofísico, 2014d).

Different types of blocks and bombs were collected from the PDC deposits along the Juive Grande and Achupashal valleys (Fig. 1B), on the NW flank of the volcano, to investigate the eruptive mechanisms driving the Vulcanian activity and the general processes of bomb formation.

3. Methods

3.1. Sampling and field observations

Bombs transported into two PDC lobes emplaced during the third explosion of the first phase of the 1 February 2014 eruption (Fig. 1B) were observed and described in two field surveys (April 2015 and September 2019) during which photos and measures of surface textural data on selected bombs were taken directly in the field. In total, we selected and preliminarily classified more than 50 bombs 17-60 cm in diameter (Table SM1) in the field, subdividing them in 4 groups based on their morphological features, such as surface characteristics, lithology and apparent density: breadcrust bombs (hereafter named BCB), cauliflower bombs (CFB), dense fragments (DB) and foliated, banded bombs (FB). Most of the collected samples are complete bombs, with every face nearly completely preserved, with the only exception of dense fragments, that in some cases possibly represent fragments of larger blocks. A subset of representative samples was then collected from each of the four groups for further analyses.

3.2. Bulk density and internal density gradients

For bulk density measurements, a total of 23 samples were measured through Archimedes' principle following the method described in Houghton and Wilson (1989). A set of 11 samples collected during the 2015 campaign (BCB1, BCB2, BCB3, BCB8, CFB1, CFB7, CFB4, CFB7, D1, D2 and TNG1) were cut into equal halves in the lab and the bulk density of the two fragments of each bomb was then measured. Other 12 bombs sampled in 2019 (BCB10, BCB14, BCB15, CFB11, CFB13, CFB16, D10) and 2015 (BCB1, BCB2, CFB1, CFB7, D2) were used to quantify the internal density gradient in each bomb. For these measurements, samples were cut into parallel-sided slabs and then subdivided into 3 to 6 pieces (of variable dimensions) cut nearly perpendicular along a core-rim transect, following macroscopic discontinuities in the vesicularity or in the texture when visible. Each piece was then weighted on a precision scale, immersed in melted paraffin to seal vesicles and weighted again once immersed within water. The bulk density of each fragments (Table SM2) is expressed as:

$$\rho_B = \omega_{AIR}/\omega_{AIR} - (\omega_{WATER} - \omega_{AIR}^{film})$$

Where ρ_B is the bulk density; ω_{AIR} is the sample weight; ω_{AIR}^{film} is the sample weight wrapped into a film; ω_{WATER} is the weight of the container filled (up to a given volume) with water and with sample wrapped immersed.

3.3. Analysis of surface fractures

The surface crack network of the bombs was investigated to characterize the surface texture of the different types of bombs and to describe the extent of post-fragmentation expansion by using digital image analysis on photos of the bomb surface directly taken in the field.

Surface fractures were first distinguished into main (or primary) and secondary fractures (Fig. SM1, supplementary material), based on the depth, width and lateral continuity of the cracks, and on the intersection relations between the different fractures. Thus, primary fractures correspond to early cracks with larger apertures and greater depths and generally represent a barrier to the smaller and shallower ones (secondary cracks). Where possible, the depth of the fracture was measured directly on the samples. To track the surface crack patterns, boundaries were outlined on each image in different colours, using the software Adobe Photoshop™. Length, width, area

and relative orientation of the main fractures were then measured on scaled images using the software ImageJ (Schneider et al., 2012). The average width of each crack defines fracture opening; in some cases, very high values were excluded because they possibly correspond to portions of the bomb for which part of the glassy rind detached during transport. The total number of cracks and the surface area of each bomb, measured from the same images, were used to define areal density for both main and secondary fractures. All individual crack orientations for each sample were combined in rose diagrams distinguishing the two types of fractures. Rose diagram bin size was set at 20° and the orientation of the main (the most frequent) direction arbitrarily set to 0°.

Areas of individual cracks were used to quantify strain (ε) accommodation by deformation on 5 breadcrust and 4 cauliflower bombs. Given the roughly prismatic shape of the bombs, the analysed surfaces of each bomb were assumed to be flat on 2D images, without introducing any correction for geometric distortion. According to the method described by Quane and Andrews (2020), both total and per-crack strains were calculated as the change in area of bombs surface (total cracks area on image, or area of an individual crack) divided by the area of surface before deformation (total area of the bombs minus total cracks area). Strain values were then plotted cumulatively distinguishing between primary and secondary fractures. In diagrams showing the cumulative strain, fractures were ordered from the largest to the smallest within each group.

3.4. Textural analysis

Textural characterization of the products (vesicle and crystal populations) was performed on backscattered electron (SEM-BSE) images of polished thin sections of 9 samples; for samples BCB1 and CFB2, two different portions of the bombs were prepared to study separately rind and core textures; samples BCB3 and FB1 were analysed defining 2 regions with different textures in each thin section (BCB3R, BCB3C and FB1a, FB1b). Images were obtained using a JEOL JSM-591LV Scanning Electron Microscope at the MEMA laboratory of the University of Florence with a 20 kV accelerating voltage and 700 pA sample current. Images were acquired from two or three areas of the rind and the core of each thin section. For each region, we collected two images at lower magnification (45x or 50x) to analyse large bubbles and phenocrysts and two to three images at higher magnification (150x or 200x) for smallest vesicles and microlites. Vesicle contours were traced manually to investigate pre-eruptive bubble conditions reconstructing, where possible, evident post-eruptive bubble coalescence phenomena or vesicle wall destruction during thin

section preparation. For crystallinity data, all the crystals smaller than 100-150 µm were arbitrarily considered here as microlites, while phenocrysts were defined as those crystals larger than 250 µm. The population between phenocrysts and microlites is defined as microphenocrysts. Area, size, and other shape or size parameters (e.g., perimeter, Feret diameter, and centroid) of both vesicles and crystals were calculated using the ImageJ software and stereological 2D to 3D conversion made using the software CSDCorrections (Higgins, 2000). Microlite areal data were normalized on a vesicle-free basis.

3.5. Petrographic and compositional features

Polished thin sections were first observed under an optical microscope and described to characterize the mineralogical assemblage and the textural heterogeneity of each sample, before using them for glass and minerals microanalyses. Major element concentrations in minerals (plagioclase, pyroxenes, and Fe-Ti oxides) and matrix glasses were measured at the Laboratoire Magmas et Volcans (LMV) in Clermont-Ferrand (France), using a CAMECA SX-100 microprobe. The operating conditions for minerals were 15 kV accelerating voltage and 10 – 12 nA beam current; whereas matrix glass measurements were performed at 15 kV accelerating voltage, 4-8 nA beam current, defocused beam of 5-10 µm size and a longer counting time. With these operating conditions and given that alkalis measurements were performed first, we should avoid significant Na migration under the electron beam (*cf.* Devine et al., 1995). For both minerals and glass measurements, we used a set of international standards. Core and rim of each phenocryst were generally analysed, while microlites were analysed close to the core.

3.6. Water content quantification by Raman spectroscopy

Water content in glasses of BCB and CFB samples was determined by Raman spectroscopy at the Laboratoire Magmas et Volcans, using a Renishaw inVia confocal micro-spectrometer equipped with a 532 nm diode-pulsed solid-state laser, a Peltier-cooled CCD detector, and a Leica DM 2500 M optical microscope. The analyses were carried out in back-scattered geometry, using a laser beam of ~5 mW focussed on the glass surface by a 100x objective, in high confocality setting (slit aperture of 20 µm); lateral and in-depth spatial resolutions were about 1 and 3 µm. The spectra were recorded from ~100 to 1350 cm^{-1} (alumino-silicate network vibration region) and from ~3000 to 3800 cm^{-1} (O-H vibration region) for 4 cycles of 30 s and 8 cycles of 30 s, respectively, using the WiRE^{TM} 4.2 software. The band areas in the water and alumino-silicate regions were

determined after subtraction of a cubic and multi-linear baseline, respectively, using PeakFit© software (see Schiavi et al. 2018, for further details about the method). Reference glasses of rhyolitic, dacitic and andesitic compositions and with different water contents (0.07 to 6.7 wt.%; Schiavi et al. 2018; Cluzel et al. 2008) were analysed several times during each analytical session and used to determine H_2O concentrations by following the external and internal calibration procedures (Schiavi et al., 2018). Being the measured water contents close to the detection limit of the method (~0.07 wt.% H_2O), the accuracy of the measurements (~20 %) was evaluated by comparison with FTIR measurements made on the same glass pockets of some selected samples using a Bruker Vertex 70 spectrometer coupled with a Hyperion microscope system (for details about the technique see Schiavi et al. 2018); the used molar absorption coefficient was 78 $Lmol^{-1}cm^{-1}$ and glass density 2450 g/L.

4. Results

4.1. Physical characteristics of bombs and blocks

The distinction of blocks and bombs into the four morphologic categories described above (dense blocks, breadcrust bombs, cauliflower bombs, and foliated, banded bombs; Fig. 2) is mainly based on their macroscopic features, such as the presence and thickness of a dense, outer glassy rind, the internal vesicularity gradient and the differences in colour and texture of the bombs.

4.1.1. Breadcrust Bombs (BCB)

BCB have a variable shape, from spherical to prismatic, with a diameter generally varying from 20 to 40 cm (Table SM1) and a smooth, glassy external rind (Fig. 2A-B) with a thickness of 10 - 20 mm. A distinctive feature of these products is the evident contrast between the dense rinds and the variably vesicular interiors (~40% of vesicularity). Vesicularity generally shows a clear gradient, with a nearly regular increase from the rind to the core. Macroscopically, primary cracks are well distinguished from secondary cracks based on intersection relationships and on the larger length, depth and opening of the former. Intersection between the cracks and the external surface results in a sharp fracture line with a dihedral angle close to 90°. Surface crack measurements were made on 14 BCB samples, for a total of 149 main cracks and 387 secondary measured fractures. Generally, crack patterns intersect at defined angles, resulting in regular sub-facets on the external surface of the bomb (Fig. 2B); in few cases, sets of primary fractures are irregular, without defining specific geometric shapes. Opening of primary cracks is not homogenous, varying between 1 and

68 mm, with a median value of 9.8 mm and a standard deviation (SD) of 11.8 mm. The distribution of the main cracks opening is presented in Fig. 3A, it shows a general decay of frequency with opening size, and presents two main modes for the intervals 0-4 and 8-12 mm. The cumulative strain measured on the surface of BCB (using crack's opening area as a proxy) is around 15-20%, reaching in one case a maximum value of 32% (Fig. 4). Strain accommodated by each individual crack ranges from around 0 up to a maximum value of 10.5%, with primary cracks accommodating in total between 77 and 86 % of the cumulative strain.

The fracture distribution on BCB surface shows a clear preferential orientation. Primary cracks intersect principally at 40-60° (Fig. 3B) with respect to the main direction (arbitrarily oriented to 0°). Similarly, secondary cracks mainly intersect at angles of 60° (12% of the total) and 300° (13%) with respect to the main direction (18%; Fig. 3B). Secondary cracks generally close in proximity of primary fractures, suggesting a time antecedence of primary with respect to secondary cracks. As shown in Fig. SM2 (supplementary material), in BCB samples the ratio of areal density of secondary with respect to primary cracks is nearly 2:1.

BCB are characterized by a rather homogenous bulk density, ranging between 1.55 x 10^3 and 1.86 x 10^3 kgm^{-3}. Bomb TNG1, representing a fragment of the external rind of a large bomb, has a density of 2.47 ± 0.07 x 10^3 kgm^{-3}, reflecting the nearly total absence of vesicles in the rind of BCB, as shown by the porosity gradient (Fig. 5A). In general, the internal density gradient of BCB (Fig. 5A) shows a passage from a dense rind (2.58 ± 0.05 x 10^3 $kg\,m^{-3}$) to a core with progressively lower density values (1.69 ± 0.13 x 10^3 kgm^{-3}). One sample (BCB15; Fig. 5A) shows a not monotonous gradient, with an intermediate portion slightly denser (1.93 ± 0.13 x 10^3 kgm^{-3}) compared to both core and rind sectors (1.66 ± 0.04 x 10^3 kgm^{-3} and 1.75 ± 0.07 x10^3 kgm^{-3}, respectively). Integration over the density profiles measured on the studied samples gives an average density of 1.88 x 10^3 kgm^{-3} for BCB. Taking a dense rock equivalent of bulk magma density of 2.76 x 10^3 kgm^{-3} (as measured for DB clasts, see below; and similar to those calculated by Garcia, 2016 at 2.71 x 10^3 kgm^{-3}), this value corresponds to an average BCB vesicularity of 32 vol.%.

4.1.2. Cauliflower bombs (CFB)

CFB, 25-60 cm in diameter (Table SM1), have ellipsoidal or prismatic flattened shapes (Fig. 2D-E) with thin, light grey, vesicular rinds (~ 50% of vesicularity) and a rough, wrinkly external surface. The bomb interior is mildly vesicular (~ 40%). A total of more than 3000 cracks (419 primary and 2906 secondary cracks) were measured for the 19 analysed bombs, typically showing two sets of

fractures on the external surface with different average length, orientation, depth and width. Opening of the main surface fractures on CFB is generally smaller than in breadcrust samples, ranging between 0.3 and 32 mm (SD: 3.67; median value: 2.73; Fig. 3A). Openings of most of secondary cracks are narrower (from 4 to 11 mm), and they are also shallower and shorter with respect to primary and secondary cracks of BCB. Frequency histograms of fractures of CFB samples display a general exponential decay from the smallest to the largest opening values, with a main mode in the interval 0-2 mm (Fig. 3A). Only 3 clasts have cracks larger than 20 mm (Fig. 3A).

Cumulative surface strain is characterized by a more curvilinear trend compared to that of BCB; total strain varies between 12 and 18%, with only one sample reaching 23% total strain (Fig. 4). Per-crack strain is lower than in BCB samples (up to 3.4%), while primary cracks accommodate between 46 and 61 % of the cumulative strain.

As shown in Figs. 2D and 3B, the primary fractures of CFB present one principal orientation (25% of cracks) that usually intersects at a variable angle with few other cracks. Similarly, the secondary fractures present a dominant orientation (16% of the total) and reciprocally intersect without any preferred orientation (Fig. 3B). Secondary fractures are largely more abundant than primary fractures, with the ratio of their respective areal densities varying between 4:1 and 10:1 (Fig. SM2).

Bulk density of CFB is lower than that of the other bombs (CFB1: 1.17 ± 0.06 x 10^3 kgm^{-3}; CFB2: 1.20 ± 0.04 x 10^3 kgm^{-3}; CFB4: 1.37 ± 0.04 x 10^3 kgm^{-3}). Only one fragment has a bulk density in the same range as BCB samples (CFB7: 1.61 ± 0.02 x 10^3 kgm^{-3}). As shown in Fig. 5B and Table SM2, the internal, core-to-rind density gradient is less marked than in BCB and slightly oscillates up to the external rind, which however shows a density generally lower than 1.80 x 10^3 kgm^{-3}. Integration over the density profiles measured on the studied samples gives an average density of 1.43 x 10^3 kgm^{-3} for CFB, corresponding to an average CFB vesicularity of 48 vol.%.

4.1.3. Dense blocks (DB)

Dense blocks are present as fragments covering a large range of sizes, from coarse lapilli to blocks (up to about 17 cm in diameter; Table SM1), with prismatic shapes, a smooth, vitreous external surface, and have no or scarce vesicularity (Fig. 2C). A quenched, glassy rim with a maximum thickness of 2 cm is sometimes evident on the external surface. Surface cracks on this zone are shallow and follow a radial jointing with a spacing of about 1 – 2 cm. The generally prismatic shape of the majority of the observed dense fragments could reflect the presence of a large, penetrative

jointing that produced a widespread re-fragmentation of large, dense blocks upon impact or during transport in the PDC. In fact, only a few fully preserved dense blocks are present in the deposits, suggesting a possible underestimation of the relative amount of this type of material with respect to the other types of bombs here described. The vesicularity of the internal portion is very low to absent. Density profile of DB fragments shows a very minor variation from the external to the inner portions (rind: 2.81 ± 0.09 x 10^3 kgm^{-3}; core: 2.70 ± 0.05 x 10^3 kgm^{-3}; Fig. 5C, Table SM2). Integration over the density profiles measured on the studied samples gives an average density of 2.76 x 10^3 kgm^{-3} for DB.

4.1.4. Foliated bombs (FB)

Vesicular portions (vesicularity: ~30%) alternating to dense glassy bands characterize FB, presenting a diameter that varies between 22 and 35cm. Single bands have regular to contorted shapes and thickness varying from a few millimetres to 40 - 50 mm. Foliation planes are present and usually continuous and parallel; however, small-scale folds are sometimes present in glassy portions, and some bands have flamed shapes. An alternation between thin vesicular and dense, glassy layers characterizes the foliation (Fig. 2F). FB show a unimodal distribution of the spacing between primary cracks, with a main mode at 2 mm (Fig. 3A). In general, values of fractures opening vary from 0.4 to 31.5 mm (SD: 4.72; median value: 2.85). The main fractures show a strong preferential orientation represented by the 30% of the total (Fig. 3A), with numerous cracks (18%) intersecting up to angles of 20°, nearly parallel to the banding. The pattern of secondary cracks follows that of the primary cracks: also in this case, the dominant orientation (21%) generally intersects with the subordinate ones (13%) at 20° (Fig. 3B), or at about 90°, possibly representing a sort of tensional cracks.

Bulk densities measured on the two foliated samples have values of 1.81 ± 0.12 x 10^3 kgm^{-3} and 1.53 ± 0.08 x 10^3 kgm^{-3}. These values correspond to vesicularities between 34 and 45 vol.%, spanning the same range of BCB-CFB clasts.

5. Petrography

Textures and mineral assemblage of three BCB samples (BCB1, BCB2 and BCB3), two CFB (CFB2 and CFB7), one DB (D1) and one FB (FB1) were investigated, also distinguishing where possible between rind and core.

All the samples share a similar mineral assemblage, which consists of plagioclase, clinopyroxene and orthopyroxene (all present as phenocrysts, microphenocrysts and microlites), tiny microlites of Fe-Ti oxides and scarce olivine phenocrysts (more abundant in CFB and FB samples). In general, the groundmass varies from glassy to intersertal. BCB shows variations in vesicularity, crystallinity and crystal size of the groundmass from the external rind (Fig. 6A, C) to the inner portion of the bomb (Fig. 6B). Both plagioclase and pyroxene phenocrysts and microphenocrysts have frequent disequilibrium textures (e.g., multiple zoning, patchy zones, resorbed rims; Fig. 6A, B), while pyroxene microlites show a Fe-rich, thin, sometimes skeletal, external rim (Fig. 6A). Glass-bearing groundmass of CFB (Fig. 6D, E) bears plagioclase microphenocrysts similar to those of BCB and rounded, partially resorbed pyroxenes (Fig. 6F). DB samples are characterized by a cryptocrystalline matrix (Fig. 6G, H, I) with a large size range for crystals (up to 2 mm). Plagioclase phenocrysts are spotted with abundant melt inclusions and have very complex zoning and clear evidence of resorption and patchy textures (Fig. 6H, I). Finally, FB show an hypocrystalline and porphyritic texture, and the different textural portions are mainly distinguished for their vesicularity.

6. Textural characteristics of bombs and blocks

6.1. Vesicle Size Distribution (VSD)

Three breadcrust bombs (BCB1, BCB2 and BCB3), two cauliflower bombs (CFB2 and CFB7) and one foliated bomb (FB1; Fig. 7) were selected for analysis of the vesicle size distribution. Separate measurements were made on the rinds and cores of BCB1, BCB3 and CFB2 and on two portions with different vesicularity of FB1 (FB1a, poorly vesicular; FB1b, vesicular). The inner portion of two additional bombs (BCB2 and CFB7) was also investigated.

In Fig. 7, the vesicle distribution measured on the bomb samples is shown in terms of volume fraction of the different class sizes (Vesicle Volume Distribution; VVD), together with the value corrected for the final vesicle coalescence. The modal values of bubble size for BCB rinds are generally lower than those for core material, and this difference maintains even after the de-coalescence procedure.

When plotted on classical VSD plots (Fig. 8), where *n* represents the vesicle population density (mm^{-4}) and *Size* the equivalent diameter in mm, cores and rinds of BCB have clearly distinct trends: VSD curves for the rinds are approximately linear, with a very steep linear segment for sizes <150 μm and vesicles not larger than about 250 μm; conversely, VSDs of cores have a more

restricted population of vesicles <100 µm and develop a population of larger vesicles characterized by a second linear segment extending up to sizes of 500-1000 µm (Fig.8A). As observed for breadcrust bombs at Guagua Pichincha (Colombier et al., 2022), vesicle number density values are however similar for both cores and rinds (Table 1), suggesting that nucleation was probably not very efficient after fragmentation and that the coarsest vesicle population possibly developed by expansion of already present vesicles. Accordingly, values of nucleation density (n_0) are not largely dissimilar between the rind and the core of a same bomb (Table 1).

Similarities in terms of volume vesicle distribution and vesicularity between rinds and cores are evident in CFB samples (Fig. 5B and 7). Bubble coalescence in this type of bombs is always important (both in rinds and cores); sizes of de-coalesced bubbles of the rind show a slightly smaller modal value compared to the core of the same sample (Fig. 7), suggesting a slightly retarded quenching for the core. The larger gap in size between de-coalesced vesicles of rind and core of BCB with respect to CFB is possibly related to a lower quenching rate for CFB, which allows a more significant pre-coalescence vesicle expansion. VSDs are defined by curved, concave upward trends (Fig. 8B), where differences between rind and core of a same sample, or between different samples, are mainly related to the largest size of vesicles (Fig. 8B) and to values of vesicle number density or n_0 (Table 1), suggesting a larger inhomogeneity for this type of bombs compared to BCB (Fig. 7 and 8).

Finally, vesicle size of FB bombs (Fig. 7) is mainly distributed at sizes smaller than 1000 µm. VSD trends are intermediate between BCB and CFB samples (Fig. 8) and values of vesicle number density and n_0 are lower with respect to the other two types of bombs (Table 1). In particular, the poorly vesicular portions (FB1a in Fig. 8C) have a linear trend although with a slope not as steep as in BCB bombs, so reflecting a coarser average size of vesicles in this population, while the VSD of the vesicle-rich portions (FB1b in Fig. 8C) are slightly curved and more irregular.

		BCB1R	BCB1C	BCB2	BCB3R	BCBC3	CFB2R	CFB2C	CFB7	FB1a	FB1b
TOTAL	1/Gτ (mm^{-1})	40.40	24.60	9.20	88.80	22.50	28.70	15.80	7.82	12.80	9.90
	n_0 (mm^{-4})	9.30E+04	1.29E+05	9.90E+03	2.68E+05	7.46E+04	5.28E+06	2.1[illegible]+04	1.84E+03	5.38E+03	3.64E+03
	3Gτ (mm)	0.074	0.122	0.326	0.034	0.133	0.105	0.1[illegible]	0.384	0.234	0.303
	BND_{fit} (mm^{-3})	2.70E+03	6.58E+03	1.08E+03	2.24E+03	3.34E+03	2.08E+[illegible]5	1.[illegible]8E+03	3.73E+02	3.91E+02	5.09E+02
SMALL VESICLES	1/Gτ (mm^{-1})	75.9	45.60	44.30	103	94.80	[illegible]60	29.70	45.60	8.76	77.50
	n_0 (mm^{-4})	2.94E+05	3.18E+05	5.31E+04	3.62E+05	4.29E+05	1.[illegible]E+07	5.05E+04	2.29E+04	5.27E+03	3.60E+04
	3Gτ (mm)	0.040	0.066	0.068	0.029	0.032	0.052	0.101	0.066	0.342	0.039
	BND_{fit} (mm^{-3})	3.87E+03	6.17E+03	1.02E+03	3.52E+03	[illegible]24E+03	2.04E+05	1.95E+03	3.27E+02	2.68E+02	4.34E+02
MEDIUM VESICLES	1/Gτ (mm^{-1})	-	-	-	49.[illegible]	-	-	-	6.76	-	6.13
	n_0 (mm^{-4})	-	-	-	[illegible]86E+04	-	-	-	5.18E+02	-	3.54E+02
	3Gτ (mm)	-	-	-	0.0[illegible]	-	-	-	0.44	-	0.49
	BND_{fit} (mm^{-3})	-	-	-	3.75E+02	-	-	-	4.63E+01	-	1.54E+01
LARGE VESICLES	1/Gτ (mm^{-1})	28.13	19.20	[illegible]47	-	11.40	16.80	8.20	1.83	12.7	4.97
	n_0 (mm^{-4})	9.23E+03	4.71E+[illegible]	2.0[illegible]4E+03	-	3.04E+03	4.60E+05	1.31E+03	2.77E+00	5.12E+03	1.85E+02
	3Gτ (mm)	0.107	0.[illegible]156	0.317	-	0.263	0.179	0.366	1.639	0.236	0.604
	BND_{fit} (mm^{-3})	3.28E+02	9.42[illegible]+02	1.08E+02	-	1.61E+02	1.03E+04	5.06E+01	2.86E-01	2.20E+02	3.10E-01

Table 1. Vesicles parameters derived from the bubble size distribution analyses; 1/Gτ: intercept of the slope; ln(n0): natural logarithm of the nuclei number density (mm^{-4}); Max. size (microlites dominant size (mm); 3Gτ: crystals average dominant size (Cashman, 1992); BND: bubble number density (mm^{-3}); Vesicularity (%).

6.2. Crystal Size Distribution (CSD)

Batch (2D) textural data and Crystal Size Distributions (CSD) of microlite and microphenocrysts in the groundmass of the different bomb types (Fig. 9) were also measured to extract quantitative information on pre- and syn-eruptive crystallization processes. Plagioclase, pyroxene (both clino- and ortho-pyroxene) and Fe-Ti oxides are the main mineralogical phases recognized and

measured; values referred to large phenocrysts (>500 μm in 2D) were not investigated in this study.

The areal number density of microlites (MND_A, Table 2, Fig. 10A) shows an overall anticorrelation with the average size for a given type of microlite (Fig. 10A), with the largest size values corresponding to plagioclase. The highest MND_A values are always associated to DB, in which pyroxene is as abundant in number as plagioclase, although having a slightly smaller average size. CFB and FB have the largest microlites and the lowest MND_A. This general trend is also well summarized by the number density values relative to the whole set of microlites, for which DB data are one order of magnitude higher compared to FB and CFB values (except sample CFB2R; Table 2).

Plagioclase is the most abundant phase in all types of bombs. On average, CSD of plagioclase microlites in BCB show two linear segments (Fig. 9) as well as two clearly distinct modes (around 200 and 50 μm) in the histograms of volume distribution (Fig. SM3, supplementary material). A similar distribution is shown by plagioclase in DB, evidencing also in this case the coexistence of two different microlite populations (modal values in the histograms of volume distribution around 20 and 120 μm; Figs. 9, SM3). Conversely, plagioclase microlites in CFB are characterized by a concave upward CSD curve, with linear segments only limited to the smaller sizes (<10-15 μm; Fig. 9). The histograms of volume distribution for these bombs (Fig. SM3) are more disturbed, with a main mode ranging between 100 and 200 μm. Crystal size distributions of pyroxene are similar for the different bomb types, with linear concave upward trends (Fig. 9). The dominant size of the finer-grained microlithic pyroxene population is smaller (half on average) than that calculated for plagioclase (Table 2; Fig. 10A). Accordingly, histograms of volume distribution for pyroxene (Fig. SM3) show irregular trends for BCB and CFB, and a bimodal trend in DB; where present, the different modes are very close one to the other and show a coarser size for the core with respect to the rind portions. Finally, oxides from all bomb types show CSD curves with very similar, gently sloping, linear to slightly concave upward trends (Fig. 9), and largely unimodal histograms of volume distribution (Fig. SM3). When calculated on a volume basis, number density values MND_V are positively correlated with the nuclei number density n_0 (Fig. 10B, Table 2), where on average the higher values of n_0 are associated to DB and, to a lower extent, BCB samples. As for MND_A data, one sample of CFB (CFB2R) does not fit this general trend.

		BCB1R	BCB2	BCB3R	BCB3C	CFB2R	CFB2C	CFB7	D1	FB1
PLAGIOCLASE	MND_A (mm^{-2})	1.53E+03	6.32E+02	2.23E+03	2.73E+03	2.43E+03	7.46E+02	7.26E+02	4.71E+03	8.12E+02
	Av size 2D (mm)	0.016	0.021	0.013	0.012	0.013	0.020	0.021	0.009	0.021
	n_0 (mm^{-4})	1.07E+07	3.91E+06	4.58E+07	3.98E+07	2.78E+07	7.73E+06	1.07E+07	2.46E+07	4.42E+06
	3Gτ (mm)	0.04	0.04	0.02	0.03	0.03	0.03	0.03	0.08	0.05
	MND_V (mm^{-3})	1.49E+05	5.81E+04	3.50E+05	3.90E+05	2.60E+05	7.37E+04	9.68E+04	6.20E+05	6.69E+04
	Groundmass xls (%)	41.20	26.30	37.30	36.90	41.20	28.4	38.40	35.60	34.30
PYROXENE	MND_A (mm^{-2})	1.31E+03	1.32E+03	1.24E+03	1.08E+03	9.43E+02	1.54E+02	2.73E+02	4.81E+03	7.06E+02
	Av size 2D (mm)	0.008	0.011	0.008	0.009	0.010	0.027	0.015	0.006	0.012
	n_0 (mm^{-4})	7.11E+07	5.82E+07	6.97E+07	9.60E+07	6.05E+06	2.47E+06	3.47E+06	8.49E+08	1.25E+07
	3Gτ (mm)	0.013	0.014	0.013	0.010	0.004	0.021	0.026	0.007	0.022
	MND_V (mm^{-3})	3.10E+05	2.80E+05	3.00E+05	3.10E+05	7.30E+05	1.70E+04	2.99E+04	2.00E+06	9.18E+04
	Groundmass xls (%)	7.90	16.00	8.90	8.30	9.40	5.30	7.80	15.40	10.90
OXIDES	MND_A (mm^{-2})	9.39E+02	5.11E+02	8.24E+02	3.02E+02	9.04E+00	1.28E+02	1.27E+02	1.52E+03	2.54E+02
	Av size 2D (mm)	0.004	0.006	0.004	0.009	0.007	0.006	0.011	0.003	0.008
	n_0 (mm^{-4})	2.91E+08	2.00E+07	1.66E+08	1.89E+07	3.79E+05	2.02E+07	3.88E+06	4.57E+08	7.07E+06
	3Gτ (mm)	0.005	0.014	0.007	0.010	0.017	0.019	0.026	0.005	0.018
	MND_V (mm^{-3})	5.04E+05	9.56E+04	3.03E+05	6.48E+04	1.82E+03	5.25E+04	2.23E+04	7.39E+05	4.29E+04
	Groundmass xls (%)	1.90	2.00	2.70	1.60	0.04	0.10	1.90	0.20	1.50
TOTAL	*MND_A (mm^{-2})*	*3.77E+03*	*2.47E+03*	*4.30E+03*	*4.12E+03*	*3.38E+03*	*1.03E+03*	*1.13E+03*	*1.10E+04*	*1.77E+03*

Table 2. Microlites parameters derived from the crystal size distribution analyses. MND_A: microlite area number density considering the crystals of the groundmass (mm^{-2}); Av size 2D: bi-dimensional mean size of crystals of the groundmass (mm); n_0: natural logarithm of the nuclei number density (mm^{-4}) related to the smallest sizes (steepest linear segment of the CSD curve); 3Gτ: crystals average dominant size related to the smallest sizes (steepest linear segment of the CSD curve; mm; Cashman, 1992); MND: microlite number density (mm^{-3}) related to the smallest sizes (steepest linear segment of the CSD curve. Xls: crystallinity degree of the groundmass, phenocrysts-free.

7. Chemical composition

All the analysed samples of the different types of bombs share a very homogeneous bulk rock composition. In the Total Alkali vs. Silica plot, as well as for other elements (Fig. 11A; Table 3) the different bombs are indistinguishable, plotting in the field of the andesite products (medium-K calc-alkaline series) erupted at Tungurahua between 1999 and 2005 (58–59 wt.% SiO_2) and close

to the range of andesites of 2006 eruptions (57.6–58.9 wt.% SiO_2; Samaniego et al., 2011; Fig. 11A).

Compared to whole-rocks, matrix glasses show higher K_2O and lower FeO_T and CaO contents (Fig. 11B, C, D), however it is worth to note that whole-rocks and matrix glasses define a single compositional trend. Matrix glass compositions clearly plot into three distinct groups (Fig. 11). The BCB samples show rhyolitic glass composition with silica contents of 72.6 ± 1.0 wt. % (Table 4); no variation is evident between the rind and the core of these samples. The matrix glass of CFB bombs shows instead a less evolved, siliceous dacitic composition (67.5 ± 1.0 wt.% SiO_2; Table 4). Similar to BCB, major element composition does not significantly vary between core and rind portions of CFB. DB matrix glasses display intermediate silica contents (69.3 ± 0.68 wt.% SiO_2; Table 4). For the sake of clarity, it is however important to observe that DB blocks present a small-scale inhomogeneity of groundmass crystal content, from glass-rich zones to microlite-rich areas (Fig. 6G, I, E, F). For this reason, the glass composition for these bombs should be carefully handled considered that these data could be mostly representative of the microlite-poor, glass-rich zones.

In Fig. 11, some selected major element concentrations of products of 2006 (Samaniego et al., 2011) are also reported. Matrix glasses of andesitic blocks and bombs of 2006 eruptive events are characterized by lower silica contents (July 14, 2006 samples: 64.7 ± 1.6 wt.% SiO_2; August 16-17, 2006 samples: 61.2 ± 0.6 wt.% SiO_2; Samaniego et al., 2011) compared to the bombs of 2014 activity (Fig. 11). On the other hand, matrix glasses of siliceous tephra and magmatic enclaves of 2006 eruptions display rhyolitic compositions (Fig. 11; Samaniego et al., 2011) closely similar to that of the 2014 BCB (Fig. 11).

wt.%	BCB	CFB	DB
SiO_2	59.20	59.34	59.40
TiO_2	0.84	0.83	0.84
Al_2O_3	16.77	16.58	16.64
Fe_2O_3	6.85	6.86	6.93
MnO	0.11	0.11	0.11
MgO	3.96	3.92	3.97
CaO	6.48	6.37	6.41
Na_2O	3.93	3.91	3.83
K_2O	1.80	1.79	1.81
P_2O_5	0.22	0.22	0.23
LOI	bdl	bdl	bdl
Total	100.10	99.84	100.02
Rb	52.67	50.39	50.18
Sr	558.87	576.33	564.69
Ba	740.21	794.67	790.00
Sc	15.92	16.18	16.51
V	165.23	166.47	169.52
Cr	93.85	92.84	99.85
Co	25.48	22.10	2[illegible]72
Ni	40.92	39.67	43.64
Y	13.04	14.14	14.32
Zr	139.75	141.05	143.27
Nb	5.54	5.98	5.20
La	18.57	18.71	18.61
Ce	38.06	37.83	36.72
Nd	19.68	19.60	19.15
Sm	3.78	3.67	4.31
Eu	1.13	1.06	0.99
Gd	3.55	3.55	3.73
Dy	2.78	2.73	2.72
Er	1.63	1.73	1.43
Yb	1.32	1.31	1.31
Th	6.39	6.01	5.91

Table 3. Whole-rock major (wt. %) and trace (ppm) elemental analyses from 2014 eruptive products measured in this study.

Sample	BCB1R					BCB1C					BCB2				
	mg12	mg13	mg8	mg4	mg2	mg17	mg24	mg16	mg27	mg25	mg4	mg.1	mg10	mg13	mg12
SiO_2	70.51	71.41	72.47	73.04	74.34	72.44	72.61	72.73	73.86	74.30	71.01	7[illegible]	71.49	72.23	72.83
TiO_2	0.83	0.86	0.67	0.89	0.74	0.60	0.62	0.69	0.80	0.48	0.80	[illegible]	1.02	0.97	0.89
Al_2O_3	14.47	13.80	12.95	12.68	13.09	12.57	12.95	12.59	12.71	12.85	12.9[illegible]	13.13	13.04	13.03	13.06
Cr_2O_3	0.01	0.07	0.05	0.00	0.03	0.00	0.01	0.01	0.00	0.04	[illegible]	0.00	0.06	bdl	bdl
FeO	2.74	2.73	2.65	2.54	2.86	2.44	2.84	2.84	2.79	2.50	3.[illegible]3	3.24	3.54	3.26	3.62
MnO	0.05	-	0.02	0.05	-	0.07	0.08	0.04	0.08	-	[illegible]12	0.06	0.12	0.07	bdl
MgO	0.30	0.27	0.31	0.30	0.31	0.29	0.27	0.26	0.23	[illegible]28	0.43	0.51	0.52	0.50	0.42
CaO	1.95	1.25	1.08	0.94	0.76	0.94	0.77	0.82	0.96	0.8[illegible]	1.45	1.63	1.35	1.45	1.55
Na_2O	4.41	4.37	3.80	3.86	3.64	3.56	3.89	3.66	3.8[illegible]	4.10	4.21	4.37	4.31	4.46	4.45
K_2O	4.46	4.78	5.10	5.15	4.96	4.94	4.97	5.[illegible]0	4.85	4.90	4.63	4.58	4.94	4.72	4.79
P_2O_5	0.18	0.12	0.00	0.23	0.08	0.10	0.1[illegible]	0.16	[illegible].03	0.12	0.30	0.25	0.25	0.24	0.30
Total	99.91	99.66	99.09	99.69	100.81	97.94	99.13	9[illegible].79	100.15	100.44	99.15	100.24	100.62	100.90	101.75

Sample	CFB2R					CFB2C						CFB7		DB1				
	mg27	mg22	mg18	mg20	mg1	mg35	mg37	mg36	mg42	mg34	mg3	mg9	mg15	mg3	mg13	mg10	mg12	
SiO_2	66.22	66.77	67.52	68.30	69.72	65.[illegible]2	65.91	66.49	67.46	67.82	66.96	67.14	67.51	68.44	68.83	69.35	70.02	
TiO_2	1.29	1.33	1.53	1.22	1.11	[illegible].52	1.47	1.35	1.42	1.41	1.45	1.36	1.69	1.26	1.33	1.33	1.25	
Al_2O_3	13.88	13.87	13.82	13.9[illegible]	[illegible].52	13.49	13.88	13.55	13.59	13.78	14.12	13.85	14.08	13.27	13.02	13.35	13.00	
Cr_2O_3	0.00	0.00	0.00	0.07	[illegible].00	0.01	0.00	0.03	0.00	0.04	0.13	-0.04	0.00	0.00	0.11	0.13	0.06	
FeO	5.72	5.34	5.06	4.72	[illegible].82	5.51	5.49	5.29	5.17	4.95	5.20	5.69	5.45	5.37	5.37	4.45	4.35	
MnO	0.17	0.02	0.12	0.11	0.03	0.03	0.19	0.12	0.03	0.15	bdl	0.11	0.14	0.01	0.06	0.11	0.13	
MgO	1.28	1.21	1.09	1.15	0.90	1.17	1.20	1.09	1.17	1.11	1.15	0.93	0.47	1.06	0.60	0.39	0.35	
CaO	3.12	3.07	2.62	2.65	1.85	3.57	3.06	2.97	2.84	2.54	2.68	3.06	2.16	2.20	1.89	1.71	1.48	
Na_2O	3.94	3.77	3.90	3.91	4.19	4.15	4.34	4.26	3.97	4.16	4.72	4.52	4.39	4.12	4.40	4.36	3.62	
K_2O	3.64	4.01	4.06	3.96	4.32	3.56	3.68	3.76	3.98	3.91	4.23	4.38	3.51	4.48	3.45	4.30	5.06	
P_2O_5	0.45	0.45	0.28	0.38	0.20	0.90	0.23	0.43	0.26	0.45	0.45	0.08	0.35	0.34	0.49	0.67	0.49	
Total	99.71	99.84	100.00	100.41	99.67	99.42	99.44	99.33	99.89	100.32	101.07	101.07	99.75	100.55	99.55	100.14	99.82	

Table 4. Selected matrix glasses major element concentrations (wt.%) from breadcrust samples (BCB1 – BCB2), cauliflower samples (CFB2 – CFB7) and dense fragment (DB1).

Water concentrations in the residual glass of selected BCB and CFB samples are reported in Table SM3 and Fig. SM4 (supplementary material). The water contents vary in a similar range for BCB

(0.07-0.27 wt.%) and CFB (0.07-0.26 wt.%) bombs. Such variability is measured even within individual bomb samples (e.g., 0.09-0.26 wt.% in BCB8, 0.13-0.26 wt.% in CFB13R). In BCB samples, rind portions generally contain slightly higher water contents than the associated cores (e.g., BCB2 and BCB10). The maximum H_2O concentrations correspond to an equilibration pressure lower than 0.5 MPa (Newman and Lowenstern, 2002), suggesting nearly complete degassing of the melt during the eruption, possibly in a very shallow plug.

Although the analysed mineral phases present important chemical compositions (as also described for the 2006 eruption; Samaniego et al., 2011), no relevant difference has been detected in plagioclase and pyroxene from all the analysed bombs. Mineral textures and compositions are presented in the Supplementary Materials (Figs. SM5, SM6; Table SM4,5,6,7).

Major elements compositions of bulk rock, groundmass glass and minerals from each type of bombs were also used for mass balance calculations to estimate the relative amounts of the different crystallized phases (Table 5). The total amount of crystallization is higher than 50 wt.% for all the bomb types, with BCB showing the largest value (nearly 67 wt.%) and CFB the lowest (54 wt.%). Crystallization is always dominated by plagioclase and minor orthopyroxene, which practically maintain the same proportions with increasing crystallization (Table 5).

	BCB	CFB	DB
Pl	44.8	35.8	41.3
Cpx	6.2	5.3	7.2
Opx	12.8	10.5	10.4
Ox	2.8	2.5	3.1
Tot	66.6	54.1	62.0
SSR	1.08	0.24	0.62

Table 5. Crystallinity results derived from mass balance calculations for the analysed bombs. SSR: sum of squares of residuals.

8. Discussion

8.1. Formation of the different types of bombs based on chemistry and textural data

The pyroclastic density current deposits in the Juive Grande and Achupashal valleys of the 1 February 2014 Tungurahua eruption have a large amount of bombs and blocks, which mainly differ for their external morphology, texture and matrix glass composition.

Benage et al. (2014) illustrated the differences in the cooling history of clasts following ballistic trajectories in the atmosphere vs. transport in a hot PDC, suggesting that this in turn influences the morphological and textural features of bombs observed in the products of Vulcanian activity. Wright et al. (2007), on the other hand, showed that the external morphology observed in the

different types of ballistic material of a Vulcanian sequence reflects the existence of primary rheological and volatile gradients in the magma plug (or magma column) occupying the conduit before an explosion. Data collected in the present study add important information to define the range of critical processes and parameters governing the large morphological and textural variability observed in the bombs and blocks associated to Vulcanian eruptions.

Cross sections through BCB evidence the large contrast in vesicularity between the dense glassy rind (similar in density to DB) and the vesicular interior, typical by definition of breadcrust bombs (Walker, 1969; Wright et al., 2007). We suggest that dense rinds possibly originated by rapid quenching, related to forced convection shortly after fragmentation, of a volatile-poor, degassed magma which prevented the development of an important vesicularity in these portions of the bombs. At the same time, the slower conductive cooling which characterized the hot bomb interior allowed a continuous growth and coalescence of gas bubbles and the expansion of bomb interiors. Most of expansion was absorbed in these bombs by the development of few primary cracks (Fig. 4), which show high values of depth, opening and total strain. We infer that cracking of the rigid external surface of these bombs was attained after the inner part had reached a vesicularity close to that presently observed in the core and ceased with the development of an important permeability, which allowed a rapid decrease of internal overpressure, so preventing further expansion (only 15-25 % of the total strain accommodated by secondary cracks; Fig. 4). Data from VSD confirm the strong decoupling of vesicle growth between rind and core of these bombs, although vesicle nucleation possibly occurred in a single event (same values of VND_A and n_0 in both the portions of the bombs), possibly coinciding with the syn-eruptive high decompression rate at the onset of the eruption. The measured total surface strain for BCB (average value 23 %) corresponds to an average volumetric strain of 36 % (calculated assuming a spherical shape). Given that the average vesicularity of BCB interior is 32 vol.%, the comparison of this value with the volumetric strain suggests that the magma which produced BCB was practically not vesicular although it still contained some dissolved volatiles. This indication agrees with the very low value of vesicularity (in the order of 5-7%) derived from density measurements on the rapidly quenched bomb rinds. We conclude that deformation mainly occurred before formation of the secondary fracture network (responsible for less than 20 % of the total strain), which possibly formed due to local overpressure that developed in sectors of the bomb (comprised between the main fractures) with lower local permeability.

The identical bulk rock and mineralogical composition shared by the three main types of blocks and bombs (DB, BCB and CFB), accompanied by important differences in the composition of the residual glass, is indicative of significant differences in the crystallization history of these products, as also confirmed by mass balance calculations (Table 5). These differences primarily result in the total extent of crystallization and, secondarily, in an increase of the Cpx/Opx ratio (and to a minor extent in an increase of the relative amount of Fe-Ti Oxides) in DB compared to the other bomb types (Table 3), possibly reflecting differences in fO_2 conditions at crystallization (Andujar et al., 2017). The evidence that plagioclase always remains the main crystallizing phase (around 66 wt.% of the total crystal content) in all the different bombs, however, confirms the primary role played by water outgassing in the crystallization of the plug, both pre- (phenocrysts) and syn-eruptively (microlites).

Groundmass crystallization of these bombs mainly occurred pre-eruptively (no important differences between rinds and cores), driven by an open system degassing (non-vesicular, low volatile pre-eruptive magma). The complex zoning/resorption pattern of plagioclase phenocrysts (Fig. 6) can be at least in part interpreted as indirect evidence of a multistage history of decompression/recompression events (Wright et al., 2023) encountered by this magma batch during its pre-eruptive ascent and stalling in the conduit or as the products of previous compositional and physical changes in the magmatic environment.

Differently from BCB, CFB have irregular surfaces and display many closely spaced cracks. The high density of surface fractures and the ellipsoidal, flattened shape of these bombs suggest a lower melt viscosity compared to BCB, which possibly affected the isotropic distribution of both primary and secondary fractures as a result of a more gradual deformation of the bombs (Fig. 4). The small thickness of the rind and the homogeneous distribution of the cracks on the entire surface of the bomb indicate slower cooling rates compared to BCB, which allowed a nearly homogeneous expansion of the bomb (no important vesicularity gradients are present inside these bombs; Fig. 5b). The average surface strain of 18% for this type of bombs resulted in a calculated volumetric strain of 28%. This value is lower than the average value of vesicularity (48 vol.%) derived from the density measurements on these bombs, suggesting that magma forming this type of bombs was characterized by a vesicularity around 20 vol.% before fragmentation and syn-eruptive expansion. Despite magma shearing, high crystal content and cracks may cause a high permeability even at very low vesicularity (Gonnermann et al, 2017; Kushnir et al., 2017; Lavallée and Kendrick, 2022), vesicularity values around 20% are generally related to very low permeability (Rust and Cashman,

2011), so suggesting nearly closed system conditions for the pre-eruptive degassing of the CFB magma. A similar indication can be derived from textural data, characterized by the lowest MND_A associated to the largest average microlite size (Fig. 10), indicating a low undercooling. All these features suggest that CFB formed by fragmentation of a portion of the magma column initially richer in volatiles and possibly at a higher temperature than the magma that originated BCB. Crystallization of this magma portion was continuous and not strongly conditioned by the final event of decompression. The low water content measured also on the rind could reflect the slow cooling and protracted degassing typical of these bombs.

Compared to the other samples, DB lack a measurable vesicularity and show the highest crystallinity, suggesting that this magma was nearly completely degassed at eruption. This is coherent with the porosity degree (< 2%) found by Gaunt et al. (2020) for the dense plug sealing the conduit during the 14 July 2013 Vulcanian explosion. Moreover, the distinctive prismatic and regular shape, together with the presence of few, narrow, polygonally arranged micro-fissures suggest that this kind of fragment was simultaneously rigid and hot at the time of eruption. Textural data reveal that groundmass crystallization of these bombs developed under a large undercooling, related to the processes of important outgassing that characterize the upper portions of a conduit plug. Several pieces of evidence, such as the presence of sieve-textured plagioclase cores and rims (Fig. 6), resorptions zones and both Fe- and Mg-rich rims in several pyroxene phenocrysts, as well as the rare presence of olivine, suggest, for BCB, the occurrence of disequilibrium processes related to multiple episodes of magma degassing/recompression during a multistep growth of the plug, accompanied or not by repeated thermal instabilities following recharge of hot mafic magma into a shallow reservoir before the final magma decompression, as suggested by Samaniego et al. (2011) or Andujar et al. (2017) for the 2006 eruptions.

Although not studied in detail in terms of their physical features, FB have zones with features typical of both BCB and CFB, so confirming that the different characteristics of the magma forming these two types of bombs possibly reflect primary differences in terms of volatiles, temperature and crystallinity. If this is the case, FB record a magmatic flow banding pre-eruptively acquired in the conduit. The low abundance of this material in the ejected products could suggest that flow banding only occurred locally, possibly in a region restricted to the interface between BCB and CFB magma types in the conduit.

Based on all these data, we suggest here that the different types of bombs recognized in the field record primary differences in the magma column from which they originated rather than

differences in the transport and depositional processes (and hence in the modality and rate of cooling). The greater amounts of BCB and DB present in the deposits would suggest in this case that coarse fragmentation mainly involved the more degassed and volatile poorer magma portions, while fine, more efficient fragmentation involved the volatile-richer magma portions, as also reflected by the generally vesicular nature of the ash (Romero et al., 2017).

8.2. Eruptive model

The data presented and discussed above give relevant insights into the different conditions of bomb formation, suggesting, by analogy with what observed by Wright et al. (2007) at Guagua Pichincha and by Gaunt et al. (2020) for the 14 July 2013 eruption at Tungurahua, that the different bomb types may be related to a pre-eruptive conduit layering and pre-fragmentation storage state (Fig. 12). In this scheme, DB samples are related to a totally degassed, possibly low-temperature portion of the system located in the shallowest portion of the conduit. BCB may represent a magma that stalled just below this dense plug. The transition zone from DB to BCB is possibly gradual, as suggested by the very low vesicularity of the BCB rims and by the measured volumetric strain of the bombs, clearly indicative of a totally post-fragmentation expansion and hence of a very low amount of residual volatiles dissolved in the pre-eruptive melt. CFB derive instead from a volatile-richer magma that occupied deeper levels in the conduit and was pre-eruptively volatile-saturated. Magma degassing in this portion of the conduit was partially pre-eruptive and under nearly closed-system conditions, as suggested by the low undercooling which prevented groundmass crystallization. In this type of conduit stratigraphy, FB could then represent those magma portions at the contact between BCB and CFB magmas mainly along the conduit margins, characterized by a large shear during magma ascent (e.g., Polacci et al., 2001). The proposed model (Fig. 12) largely confirms what already observed by Wright et al. (2007) for the 1999 Guagua Pichincha dacitic eruption, by Giachetti et al. (2011) for the 1997 andesitic Vulcanian explosions at Montserrat, by Bain et al. (2019) for the 2004-2010 andesitic eruptions of Galeras and by Gaunt et al. (2020) for the 14 July 2013 Vulcanian eruption at Tungurahua. Worth to note, while dense and breadcrust bombs were certainly produced in the above referenced eruptive products, no cauliflower bombs have been clearly described, so confirming that the processes involved in the formation of this type of bombs are not composition-dependent, but possibly require specific conditions at the time of eruption.

The possible model for the internal structure of the plug discussed above clearly applies to the plug present at the moment of ejection of the different bombs here analysed, and hence just before the third, and largest, Vulcanian explosion occurred during the rapid series of 3 explosions of the February 1, 2014 event (respectively occurred at 22:12, 22:32 and 22:39). The very rapid succession of explosions clearly excludes the possibility of a massive disruption of the plug during each event, followed by its rapid re-emplacement. In fact, the need of a high feeding rate allowing the formation of a magma plug in very short times conflicts with the characteristic time needed for an important outgassing and crystallization of the new magma forming the plug. Wright et al. (2007) estimated a refilling time varying between 7 days to 12 h at ascent rates 0.5 cm/and 6 cm/s for the 1999 eruption at Guagua Pichincha. Similarly, we have here preliminarily tried to estimate the timing of magma ascent considering the dominant size of plagioclase microlites and average growth rates for crystals in dacites, suggesting times of crystallization in the order of 1-10 days. For all these considerations, we suggest here that the first two explosions only partially disrupted small portions of the pre-eruptive conduit plug, that was instead largely removed by the third, largest explosion. This was indeed followed by a short phase of sustained activity and by a strombolian-like activity which protracted for several days, so suggesting the passage to open-conduit conditions.

8.3. A general origin for cauliflower bombs

All the morphological, textural and compositional data presented above are useful to depict a more precise definition of the term cauliflower bombs. In fact, while breadcrust bombs are a common category that has a clear definition in the literature in terms of shape, pattern of external fracturing and presence of a sharp contrast between a dense, glassy rind and a variably vesicular core (e.g., Fisher and Schimncke, 1984; Walker, 1969; Wright et al., 2007), cauliflower bombs still lack a clear definition in the literature. Most of the authors describe these bombs as scoriaceous clasts with a rounded shape and a convolute, rough surface fractured by an irregular network of small cracks (Alvarado and Soto, 2002; Miyabuchi et al., 2006; Rosseel et al., 2006). The main features generally used by authors for distinguishing between cauliflower and breadcrust bombs lay in the external smooth, dense, glassy surface of the latter and in the supposed more mafic composition of cauliflower bombs (Alvarado and Soto, 2002; Miyabuchi et al., 2006).

Our data may contribute to reveal the significance of cauliflower bombs in many eruptions. First, there is no evidence of magma-water interaction in the recent Vulcanian eruptions of Tungurahua (at least since 1999 event; e.g., Eychenne et al., 2012, 2013; Gaunt et al., 2020), so that a primary role of these processes in determining the formation of this type of bombs can be ruled out. The clear coexistence of breadcrust and cauliflower bombs with the same magma composition also suggests a minor role of composition in the final formation of these bombs. Textural data possibly give a key for defining that differences in magma viscosity related to the crystal cargo of the magma could play a primary control on the final characteristics of the bombs. While the observed differences in composition of the residual melt do not cause important differences in the melt viscosity (e.g., viscosity of anhydrous residual melt at 800°C, calculated according to Giordano et al., 2008, varies in the range $10^{9.81}$-$10^{10.25}$ Pa·s for the different bombs), the lower microlite content (in volume and in number) of CFB and especially their crystal size distribution, characterized by larger crystals and by a poorly varied crystal population in terms of size (Fig. 10, Table 2, Table 5), could result in a significantly lower effect of the crystal cargo on increasing the final magma viscosity compared to the other bombs (Cimarelli et al., 2011; Gaudio, 2014). While the external morphology and the amount of BCB volumetric expansion compared to measured vesicularity suggests a pre-eruptive state for BCB magma characterized by a low temperature and strongly outgassed conditions, the same type of data for CFB confirm the presence of an important pre-eruptive vesicularity for this magma portion and a more plastic state, possibly also related to a higher temperature. In this context, the conditions for CFB formation would be mainly related to (even small) differences in magma viscosity along the fragmented plug. The lower cooling rates apparently experienced by these bombs (as suggested by the absence of a smooth, obsidian-likeglassy rind) could suggest a lower degree of interaction with cold air during their transfer to the surface, so indicating that transport in PDCs could be a necessary (although not sufficient) condition for their formation (Benage et al., 2014).

9. Conclusions

The study of coarse juvenile material ejected during vulcanian or other discrete, pulsating eruptions characterized by the periodic stallation of magma at shallow level in a conduit/dyke system represents a fundamental tool to investigate the pre-eruptive conditions of these events. The presented data demonstrate that the textural features of this material, although partially acquired after fragmentation, still record pre-eruptive conditions, and well report on the existing

short-scale lateral and vertical heterogeneities in crystallinity and rheology typical of conduit systems of limited dimensions associated with eruptions of limited flow rate.

The large textural and compositional variability observed in the bombs of the studied eruption does not evidence any important interaction with newly arrived fresh magma, and the gradational variations observed between the different types of bombs/blocks can be well correlated with the geometry of a pre-existing, partially to completely degassed plug occupying the upper portions of the conduit. Despite this, the increase in seismicity recorded in the 2 days preceding the eruption (Romero et al., 2017) suggests a progressive pressurization of the system possibly related to the arrival of new magma, whose fragmentation could have triggered the (passive) disruption and propelled the dispersion of the plug. Direct evidence of fresh magma participating in the eruption should therefore be sought in the fine material (mostly ash, not examined in this work) rather than in the bomb/block population (Battaglia et al., 2019).

The strict association of cauliflower bombs with other bomb types (breadcrust, foliated, dense blocks) may help clarify the formation conditions for this peculiar type of clasts, generally related to a specific mechanism of bomb production (i.e. phreatomagmatic activity) or to specific compositional features of the magma, suggesting that they represent portions of still hot, partially vesicular (up to 20% pre-fragmentation vesicularity), plastic magma that partially continues to degas and expand after fragmentation. Due to the rare occurrence of this type of bombs in typical vulcanian eruptions, we can infer that these conditions are not very common in a degassed plug, and could be possibly related to the development of an anomalously low permeability in the upper portions of the plug, which does not favor efficient outgassing of the inner portion of the upper conduit system. Further comparisons with the gas flux from the vent area preceding these eruptions could help clarify this hypothesis.

Acknowledgments

The authors would like to thank Jean-Luc Devidal for his help with microprobe analysis and Laura Chiarantini for technical support in collecting BSE images.

References

Alvarado, G. E., & Soto, G. J. (2002). Pyroclastic flow generated by crater-wall collapse and outpouring of the lava pool of Arenal Volcano, Costa Rica. Bulletin of volcanology, 63(8), 557-568.

Andújar, J., Martel, C., Pichavant, M., Samaniego, P., Scaillet, B., & Molina, I. (2017). Structure of the plumbing system at Tungurahua volcano, Ecuador: insights from phase equilibrium experiments on July–August 2006 eruption products. Journal of Petrology, 58(7), 1249-1278.

Bablon, M., Quidelleur, X., Samaniego, P., Le Pennec, J. L., Lahitte, P., Liorzou, C., ... & Hidalgo, S. (2018). Eruptive chronology of Tungurahua volcano (Ecuador) revisited based on new K-Ar ages and geomorphological reconstructions. Journal of Volcanology and Geothermal Research, 357, 378-398.

Bain, A. A., Calder, E. S., Cortés, J. A., Cortés, G. P., & Loughlin, S. C. (2019). Textural and geochemical constraints on andesitic plug emplacement prior to the 2004–2010 vulcanian explosions at Galeras volcano, Colombia. Bulletin of Volcanology, 81, 1-25.

Battaglia, J., Hidalgo, S., Bernard, B., Steele, A., Arellano, S., & Acuña, K. (2019). Autopsy of an eruptive phase of Tungurahua volcano (Ecuador) through coupling of seismo-acoustic and SO2 recordings with ash characteristics. Earth and Planetary Science Letters, 511, 223-232.

Benage, M. C., Dufek, J., Degruyter, W., Geist, D., Harpp, K., & Rader, E. (2014). Tying textures of breadcrust bombs to their transport regime and cooling history. Journal of volcanology and geothermal research, 274, 92-107.

Bernard, J., Kelfoun, K., Le Pennec, J. L., & Vargas, S. V. (2014). Pyroclastic flow erosion and bulking processes: comparing field-based vs. modelling results at Tungurahua volcano, Ecuador. Bulletin of volcanology, 76(9), 858.

Cashman, K. V. (1992). Groundmass crystallization of Mount St. Helens dacite, 1980–1986: a tool for interpreting shallow magmatic processes. Contributions to Mineralogy and Petrology, 109(4), 431-449.

Cashman, K. V., Thornber, C. R., Pallister, J. S. (2008). From dome to dust: Shallow crystallization and fragmentation of conduit magma during the 2004-2006 dome extrusion of Mount St. Helens, Washington (No. 1750-19, pp. 387-413). US Geological Survey.

Cimarelli, C., Costa, A., Mueller, S., & Mader, H. M. (2011). Rheology of magmas with bimodal crystal size and shape distributions: Insights from analog experiments. Geochemistry, Geophysics, Geosystems, 12(7).

Cioni, R., Pistolesi, M., & Rosi, M. (2015). Plinian and SubPlinian eruptions. In The encyclopedia of volcanoes (pp. 519-535). Academic Press.

Cluzel, N., Laporte, D., Provost, A., Kannewischer, I. (2008). Kinetics of heterogeneous bubble nucleation in rhyolitic melts: implications for the number density of bubbles in volcanic conduits and for pumice textures. Contrib Mineral Petrol, 156(6), 745-763.

Cole, P. D., Fernandez, E., Duarte, E., & Duncan, A. M. (2005). Explosive activity and generation mechanisms of pyroclastic flows at Arenal volcano, Costa Rica between 1987 and 2001. Bulletin of Volcanology, 67(8), 695-716.

Colombier, M., Bernard, B., Wright, H., Le Pennec, J. L., Cáceres, F., Cimarelli, C., Heap, M.J., Samaniego, P., Vasseur, J., Dingwell, D. B. (2022). Conduit processes in crystal-rich dacitic magma and implications for eruptive cycles at Guagua Pichincha volcano, Ecuador. Bulletin of Volcanology, 84(12), 105.

Devine, J. D., Gardner, J. E., Brack, H. P., Layne, G. D., & Rutherford, M. J. (1995). Comparison of microanalytical methods for estimating H2O contents of silicic volcanic glasses. American Mineralogist, 80(3-4), 319-328.

Douillet, G. A., Tsang-Hin-Sun, È., Kueppers, U., Letort, J., Pacheco, D. A., Goldstein, F., ... & Robin, C. (2013). Sedimentology and geomorphology of the deposits from the August 2006 pyroclastic density currents at Tungurahua volcano, Ecuador. Bulletin of volcanology, 75(11), 765.

Druitt, T. H., Young, S. R., Baptie, B., Bonadonna, C., Calder, E. S., Clarke, A. B., Cole, P. D., Harford, C.L., Herd, R.A., Luckett, R., Ryan, G., Voight, B. (2002). Episodes of cyclic Vulcanian explosive activity with fountain collapse at Soufrière Hills Volcano, Montserrat. Memoirs-Geological Society of London, 21, 281-306.

Eychenne, J., Le Pennec, J. L., Ramon, P., & Yepes, H. (2013). Dynamics of explosive paroxysms at open-vent andesitic systems: high-resolution mass distribution analyses of the 2006 Tungurahua fall deposit (Ecuador). Earth and Planetary Science Letters, 361, 343-355.

Eychenne, J., Le Pennec, J. L., Troncoso, L., Gouhier, M., & Nedelec, J. M. (2012). Causes and consequences of bimodal grain-size distribution of tephra fall deposited during the August 2006 Tungurahua eruption (Ecuador). Bulletin of Volcanology, 74, 187-205.

Fisher, R. V., & Schmincke, H. U. (1984). Pyroclastic rocks. Springer, Heidelberg, 474

García Moreno, J. D. (2016). Mapeo y determinación de parámetros físicos de las corrientes de densidad piroclásticas producidas por el volcán Tungurahua producidas desde el 2006. 196 hojas. Quito : EPN.

Gaudio, P. D. (2014). Rheology of bimodal crystals suspensions: Results from analogue experiments and implications for magma ascent. Geochemistry, Geophysics, Geosystems, 15(1), 284-291.

Gaunt, H. E., Burgisser, A., Mothes, P. A., Browning, J., Meredith, P. G., Criollo, E., & Bernard, B. (2020). Triggering of the powerful 14 july 2013 vulcanian explosion at tungurahua volcano, Ecuador. Journal of Volcanology and Geothermal Research, 392, 106762.

Giachetti, T., Burgisser, A., Arbaret, L., Druitt, T. H., & Kelfoun, K. (2011). Quantitative textural analysis of Vulcanian pyroclasts (Montserrat) using multi-scale X-ray computed microtomography: comparison with results from 2D image analysis. Bulletin of Volcanology, 73, 1295-1309.

Giordano, D., Russell, J. K., & Dingwell, D. B. (2008). Viscosity of magmatic liquids: a model. Earth and Planetary Science Letters, 271(1-4), 123-134.

Gonnermann, H. M., Giachetti, T., Fliedner, C., Nguyen, C. T., Houghton, B. F., Crozier, J. A., & Carey, R. J. (2017). Permeability during magma expansion and compaction. Journal of Geophysical Research: Solid Earth, 122(12), 9825-9848.

Hall, M. L., Robin, C., Beate, B., Mothes, P., & Monzier, M. (1999). Tungurahua Volcano, Ecuador: structure, eruptive history and hazards. Journal of volcanology and Geothermal Research, 91(1), 1-21.

Hall, M. L., Steele, A. L., Bernard, B., Mothes, P. A., Vallejo, S. X., Douillet, G. A., ... & Ruiz, M. C. (2015). Sequential plug formation, disintegration by Vulcanian explosions, and the generation of granular Pyroclastic Density Currents at Tungurahua volcano (2013–2014), Ecuador. Journal of Volcanology and Geothermal Research, 306, 90-103.

Hall, M. L., Steele, A. L., Mothes, P. A., & Ruiz, M. C. (2013). Pyroclastic density currents (PDC) of the 16–17 August 2006 eruptions of Tungurahua volcano, Ecuador: Geophysical registry and characteristics. Journal of Volcanology and Geothermal Research, 265, 78-93.

Hammer, J. E., Cashman, K. V., Hoblitt, R. P., Newman, S. (1999). Degassing and microlite crystallization during pre-climactic events of the 1991 eruption of Mt. Pinatubo, Philippines. Bulletin of Volcanology, 60(5), 355-380.

Heiken, G. (Ed.). (2006). Tuffs: their properties, uses, hydrology, and resources (Vol. 408). Geological Society of America.

Higgins, M. D. (2000). Measurement of crystal size distributions. American mineralogist, 85(9), 1105-1116.

Hoblitt, R. P., & Harmon, R. S. (1993). Bimodal density distribution of cryptodome dacite from the 1980 eruption of Mount St. Helens, Washington. Bulletin of Volcanology, 55(6), 421-437.

Houghton, B. F., & Wilson, C. J. N. (1989). A vesicularity index for pyroclastic deposits. Bulletin of volcanology, 51(6), 451-462.

Kelfoun, K., Samaniego, P., Palacios, P., & Barba, D. (2009). Testing the suitability of frictional behaviour for pyroclastic flow simulation by comparison with a well-constrained eruption at Tungurahua volcano (Ecuador). Bulletin of volcanology, 71(9), 1057.

Kushnir, A. R., Martel, C., Champallier, R., & Arbaret, L. (2017). In situ confirmation of permeability development in shearing bubble-bearing melts and implications for volcanic outgassing. Earth and Planetary Science Letters, 458, 315-326.

Instituto Geofísico, E. P. N.: Informe especial del volcán Tungurahua no. 01, available at: http://www.igepn.edu.ec/, last access: 9 February 2014a.

Instituto Geofísico, E. P. N.: Informe especial del volcán Tungurahua no. 02, available at: http://www.igepn.edu.ec/, last access: 9 February 2014b.

Instituto Geofísico, E. P. N.: Informe especial del volcán Tungurahua no. 04, available at: http://www.igepn.edu.ec/, last access: 9 February 2014c.

Instituto Geofísico, E. P. N.: Informe especial del volcán Tungurahua no. 05, http://www.igepn.edu.ec/, last access: 9 February 2014d.

Lavallée, Y., & Kendrick, J. E. (2022). Strain localization in magmas. Reviews in Mineralogy and Geochemistry, 87(1), 721-765.

Lorenz, V. (1973). On the formation of maars. Bulletin volcanologique, 37(2), 183-204.

Lorenz, V. (1987). Phreatomagmatism and its relevance. Chemical Geology, 62(1-2), 149-156.

Martí, J., Planagumà, L., Geyer, A., Canal, E., & Pedrazzi, D. (2011). Complex interaction between Strombolian and phreatomagmatic eruptions in the Quaternary monogenetic volcanism of the Catalan Volcanic Zone (NE of Spain). Journal of Volcanology and Geothermal Research, 201(1-4), 178-193.

Miyabuchi, Y., Watanabe, K., & Egawa, Y. (2006). Bomb-rich basaltic pyroclastic flow deposit from Nakadake, Aso Volcano, southwestern Japan. Journal of volcanology and geothermal research, 155(1-2), 90-103.

Morrissey, M. M. & Mastin, L. G. (2000). Vulcanian Eruptions. In Encyclopedia of Volcanoes, ed. Sigurdsson, H.. San Diego, CA: Academic Press, 463–475.

Nairn, I. A., & Self, S. (1978). Explosive eruptions and pyroclastic avalanches from Ngauruhoe in February 1975. Journal of volcanology and geothermal research, 3(1-2), 39-60.

Németh, K., & Cronin, S. J. (2008). Volcanic craters, pit craters and high-level magma-feeding systems of a mafic island-arc volcano: Ambrym, Vanuatu, South Pacific. Geological Society, London, Special Publications, 302(1), 87-102.

Németh, K., & Kósik, S. (2020). Review of explosive hydrovolcanism. Geosciences, 10(2), 44.

Neuberg, J. W., Collinson, A. S., Mothes, P. A., Ruiz, M. C., & Aguaiza, S. (2018). Understanding cyclic seismicity and ground deformation patterns at volcanoes: intriguing lessons from Tungurahua volcano, Ecuador. Earth and Planetary Science Letters, 482, 193-200.

Newman, S., & Lowenstern, J. B. (2002). VolatileCalc: a silicate melt–H2O–CO2 solution model written in Visual Basic for excel. Computers & Geosciences, 28(5), 597-604.

Polacci, M., Papale, P., & Rosi, M. (2001). Textural heterogeneities in pumices from the climactic eruption of Mount Pinatubo, 15 June 1991, and implications for magma ascent dynamics. Bulletin of Volcanology, 63, 83-97.

Quane, S. L., & Andrews, B. J. (2020). Breadcrust bubbles: Ash particles recording post-fragmentation brittle-ductile deformation. Geology, 48(12), 1205-1209.

Romero, J. E., Douillet, G. A., Vallejo Vargas, S., Bustillos, J., Troncoso, L., Díaz Alvarado, J., & Ramón, P. (2017). Dynamics and style transition of a moderate, Vulcanian-driven eruption at Tungurahua (Ecuador) in February 2014: pyroclastic deposits and hazard considerations. Solid Earth, 8(3), 697-719.

Rosseel, J. B., White, J. D. L., & Houghton, B. F. (2006). Complex bombs of phreatomagmatic eruptions: Role of agglomeration and welding in vents of the 1886 Rotomahana eruption, Tarawera, New Zealand. Journal of Geophysical Research: Solid Earth, 111(B12).

Rust, A. C., & Cashman, K. V. (2011). Permeability controls on expansion and size distributions of pyroclasts. Journal of Geophysical Research: Solid Earth, 116(B11).

Samaniego, P., Le Pennec, J. L., Robin, C., & Hidalgo, S. (2011). Petrological analysis of the pre-eruptive magmatic process prior to the 2006 explosive eruptions at Tungurahua volcano (Ecuador). Journal of Volcanology and Geothermal Research, 199(1-2), 69-84.

Schiavi, F., Bolfan-Casanova, N., Withers, A.C., Médard, E., Laumonier, M., Laporte, D., Flaherty, T., Gomez-Ulla, A., 2018. Water quantification in silicate glasses by Raman spectroscopy: correcting for the effects of confocality, density and ferric iron. Chem. Geol. 483, 312–331.

Schneider, C.A., Rasband, W.S., Eliceiri, K.W. "NIH Image to ImageJ: 25 years of image analysis". Nature Methods 9, 671-675, 2012.

Self, S., Wilson, L., & Nairn, I. A. (1979). Vulcanian eruption mechanisms. Nature, 277, 440-443.

Sparks, R. S. J. (1997). Causes and consequences of pressurisation in lava dome eruptions. Earth and Planetary Science Letters, 150(3-4), 177-189.

Turcotte, D. L., Ockendon, H., Ockendon, J. R., & Cowley, S. J. (1990). A mathematical model of vulcanian eruptions. Geophysical Journal International, 103(1), 211-217.

Walker, G. P. L. (1969). The breaking of magma. Geological Magazine, 106(2), 166-173.

Walker, G. P. L. (1982). Eruptions of andesitic volcanoes. R.S Thorpe (Ed.), Andesites: orogenic andesites and related rocks, Wiley, New York, 403-413.

Woods, A. W. (1995). The dynamics of explosive volcanic eruptions. Reviews of geophysics, 33(4), 495-530.

Wright, H., Cashman, K. V., Rosi, M., & Cioni, R. (2007). Breadcrust bombs as indicators of Vulcanian eruption dynamics at Guagua Pichincha volcano, Ecuador. Bulletin of Volcanology, 69(3), 281-300.

Wright, H. M. N., Cioni, R., Cashman, K. V., Mothes, P., & Rosi, M. (2022). Decompression and degassing, repressurization, and regassing during cyclic eruptions at Guagua Pichincha volcano, Ecuador, 1999–2001. Bulletin of Volcanology, 85(2), 12.

Http://www.ssd.noaa.gov/VAAC/messages.html

Figures Captions

Fig. 1. A. Location map of Tungurahua volcano in Ecuadorean Andes. Active volcanoes are reported with black triangle. B. PDCs distribution of the deposit of February 1, 2014 eruption and bombs sampling sites (white circles); the yellow circle indicates the RETU station position (modified from Hall et al., 2015).

Fig. 2. Volcanic bomb texture at Tungurahua volcano: A – B. breadcrust bombs (BCB1, BCB3); C. dense fragments (D1, D2); D – E. cauliflower bombs (CFB1, CFB4); F. foliated, banded bombs (FB1).

Fig. 3. A. Frequency histogram of cracks opening for all breadcrust, cauliflower and foliated bombs investigated. N is the number of effective main fractures measured. Spacing range is wider in BCB samples. The most frequent openings are 4 and 12 mm in breadcrust bomb; in CFB and FB clasts, the main mode is at 2 mm. B. Main and secondary cracks orientation patterns for both all breadcrust and cauliflower samples. In breadcrust bombs, main cracks measured are 149 and secondary cracks are 387. In cauliflower samples, main cracks measured are 419 and secondary cracks are 2906. 65 main cracks and 168 secondary cracks are measured in foliated bombs.

Fig. 4. Total strain ε (%) calculated for 5 breadcrust bombs (blue lines) and 4 cauliflowers samples (red dashed lines). Primary cracks are plotted on left; fractures areas are in descending order distinguishing between primary and secondary cracks. Strain values are cumulative.

Fig. 5. Internal density gradient of (A) 5 breadcrust samples, (B) 5 cauliflower-shaped bombs and (C) 2 dense fragments plotted *vs* distance (from cores to rinds of the bombs) normalized to 1, in order to facilitate the comparison.

Fig. 6. Groundmass texture of: (A) rind and (B) core of BCB1 sample and (C) rind of BCB3 sample. (D), (E) and (F) show the groundmass textures of CFB samples. For both BCB and CFB samples, disequilibrium textures as multiple zoning, resorption surface and patchy textures for plagioclase and few pyroxene crystals are highlighted in the images. Disequilibrium textures in microphenocrysts are similar in BCB and CFB samples (C – D). In (G), (H) and (I) the cryptocrystalline textures of the dense samples are represented at high and low magnification.

Fig. 7. Glass-referenced (i.e., crystal-free) vesicles volume distributions of selected measured samples: breadcrust bombs (BCB1R, BCB1C, BCB2C, BCB3R, BCB3C), cauliflower samples (CFB2R, CFB2C, CFB7C), foliated-banded bombs (FB1a, FB1b). The suffix *dec* refers to vesicle size distributions in which vesicles were manually decoalesced; R: rim of the bomb; C: core of the bomb.

Fig. 8. Vesicle size distribution for the (A) breadcrust bombs, (B) cauliflower bombs, (C) foliated-banded bombs. A magnification of vesicle size distributions for sizes lower than 160 µm is reported in the upper right boxes.

Fig. 9. Crystal (< 100 µm) size distribution in term of number density (n) for (A) plagioclase, (B) pyroxene and (C) oxides of bombs analysed in this study.

Fig. 10. Textural parameters for the different types of bombs and blocks and the three main mineral types. (A) Microlites averages sizes vs areal number density of microlites (MND_A). A negative correlation is shown for plagioclase, pyroxene and oxides for all the different type of bombs. (B) The nuclei number density (n_0) vs number density values on volume basis, (MND_V) plot is characterized by a positive correlation; the higher values of n_0 for all the three mineral types are shown by DB bombs.

Fig. 11. TAS and selected major elements diagrams for whole-rock samples and matrix glass of bombs erupted during the February 2014 Vulcanian eruption at Tungurahua volcano. For comparison, whole-rock and matrix glass compositions of both andesitic and siliceous products from the eruption of August 16-17, 2006 are reported (data from Samaniego et al., 2011). A. Total alkali, B. K_2O, C. FeO, D. CaO plotted versus silica (wt.%). WR, whole rock. T&B, tephra and bombs; T&E, tephra and enclaves; BCB, breadcrust bombs; CFB, cauliflower bombs; DB, dense blocks.

Fig 12. Schematic model of the magma conduit layering (not in scale) linked to the 1 February 2014 Vulcanian event at Tungurahua volcano. Dense bombs (DB) represent the totally degassed plug at the uppermost portions of the rising magma into the conduit. Breadcrust bombs (BCB) are related to a partially degassed magma located just below the dense plug. CFB (cauliflower bombs) occupy the deepest levels of the pre-eruptive conduit stratigraphy, representing a volatile-rich magma. Possibly, foliated bombs (FB) represent magma at the transitional contact between BCB and CFB and located in the marginal parts of the conduit.
The tip of the arrow indicates the highest values related to the different parameters reported in the figure.

Author Statement

A.F. and R.C. coordinated, wrote, and organized the manuscript, figures and tables. R.C., B.B. and M.P. are responsible for sample collection and field analyses. A.F and P.S. carried out glass and mineral chemical analysis via EPMA, and BSE imaging. Density measurements, textural and morphological analysis were carried out by A.F. with contributions from R.C. F.S. carried out water contents measurements by Raman spectroscopy. All the authors participated in the interpretation of results and finalization of the manuscript.

Highlights

- Rheological zoning in the conduit is recorded in juvenile bombs and blocks
- Cauliflower bomb (CFB) formation does not depend on composition
- Condition for CFB formation related to differences in magma viscosity
- Magma-water interaction does not play a primary role in the formation of CFB

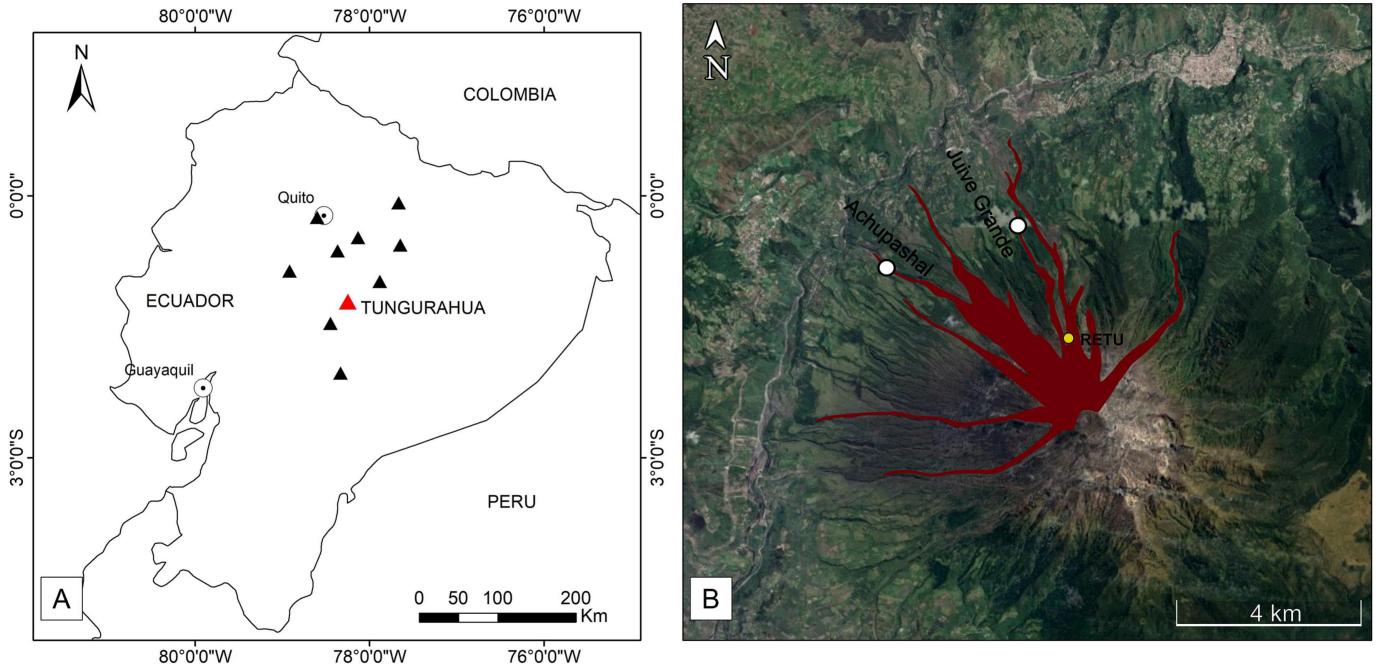
80°0'0"W
78°0'0"W
76°0'0"W
N
COLOMBIA
0°0'0"
Quito
ECUADOR
TUNGURAHUA
Guayaquil
3°0'0"S
PERU
A
0 50 100 200
Km
Juive Grande
Achupashal
RETU
B
4 km

Figure 1

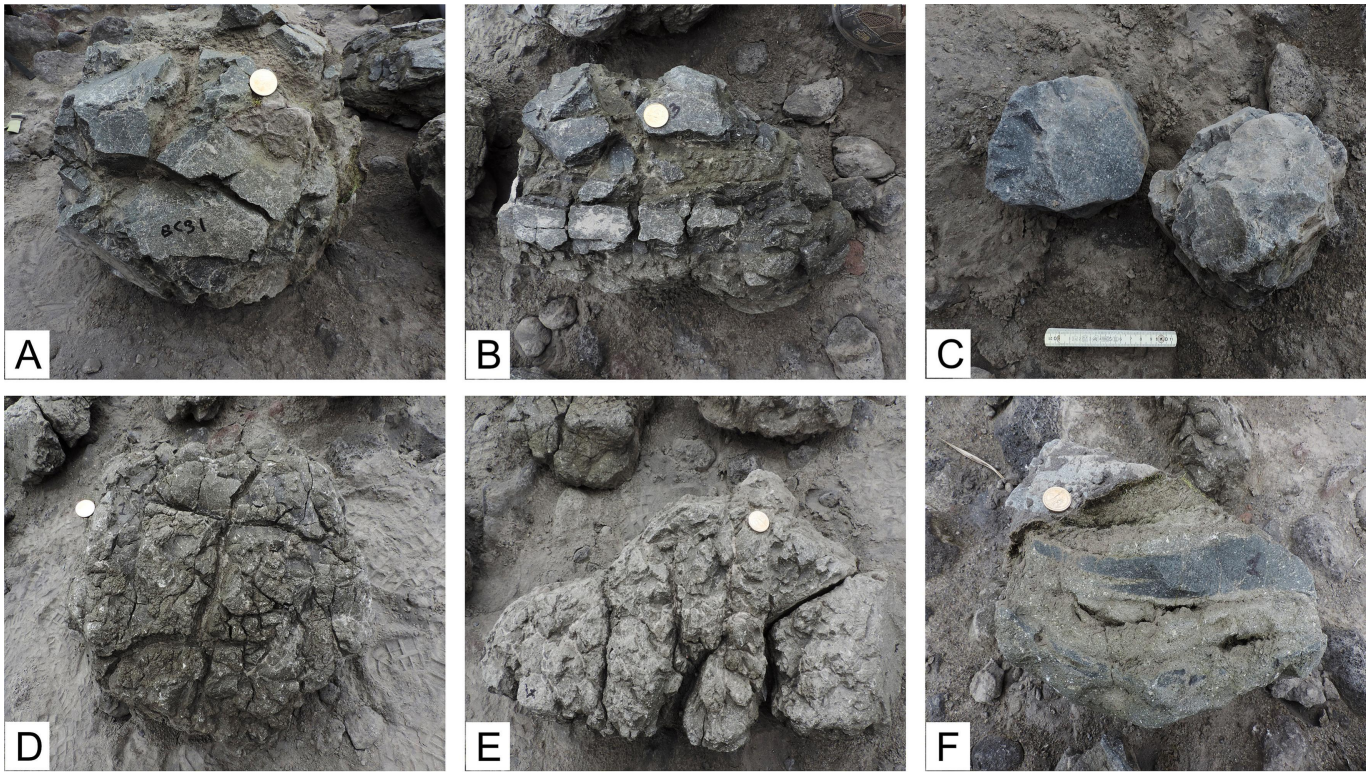

Figure 2

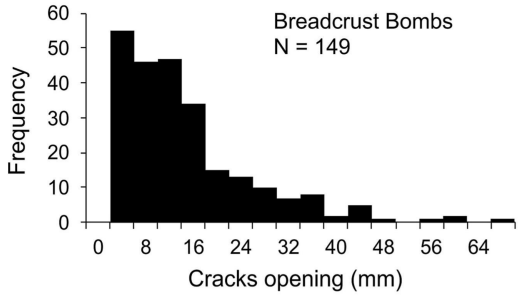
Breadcrust Bombs
N = 149
Frequency
Cracks opening (mm)

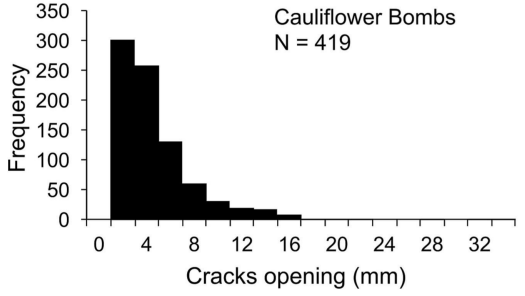
Cauliflower Bombs
N = 419
Frequency
Cracks opening (mm)

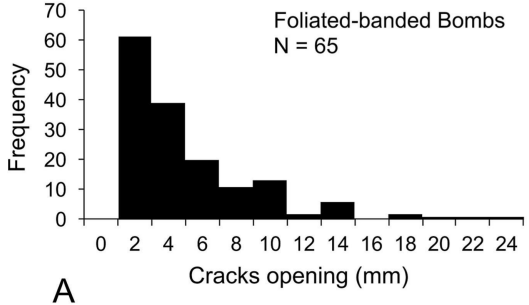
Foliated-banded Bombs
N = 65
Frequency
Cracks opening (mm)

A

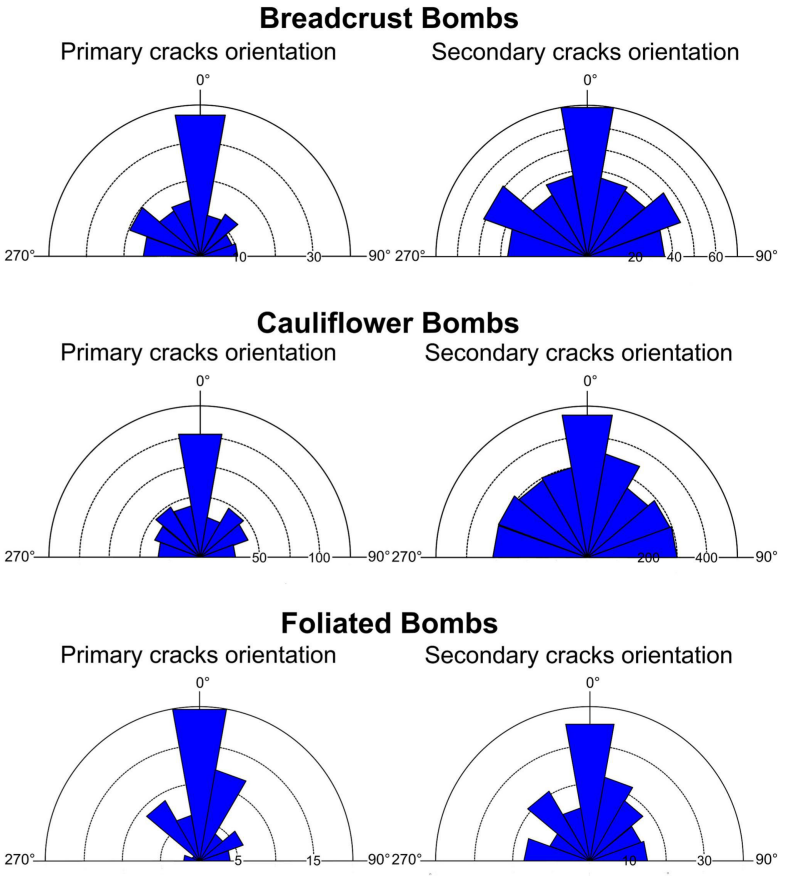
Breadcrust Bombs
Primary cracks orientation
Secondary cracks orientation
Cauliflower Bombs
Primary cracks orientation
Secondary cracks orientation
Foliated Bombs
Primary cracks orientation
Secondary cracks orientation

B

Figure 3

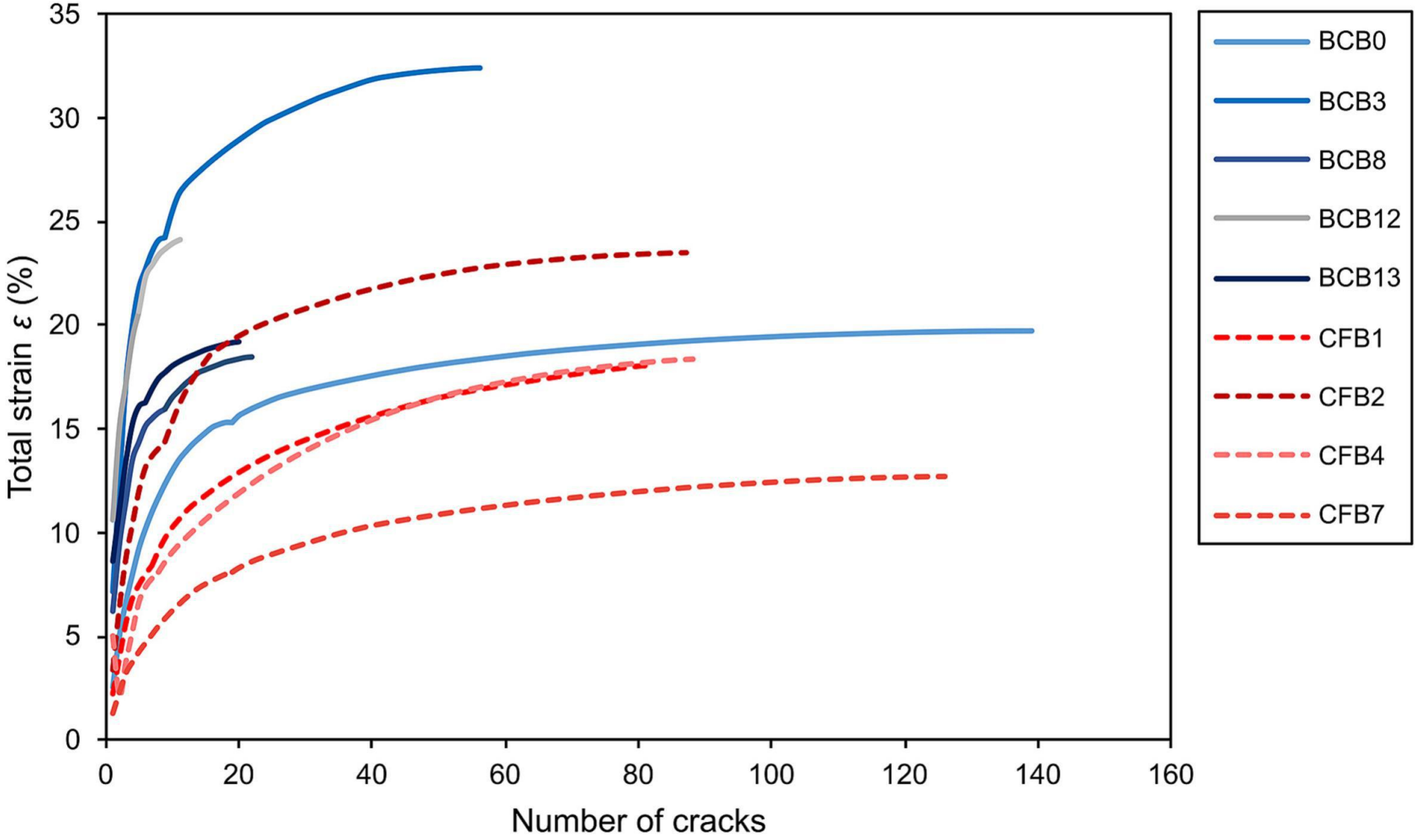
Total strain ε (%)
Number of cracks
0
5
10
15
20
25
30
35
0
20
40
60
80
100
120
140
160
BCB0
BCB3
BCB8
BCB12
BCB13
CFB1
CFB2
CFB4
CFB7

Figure 4

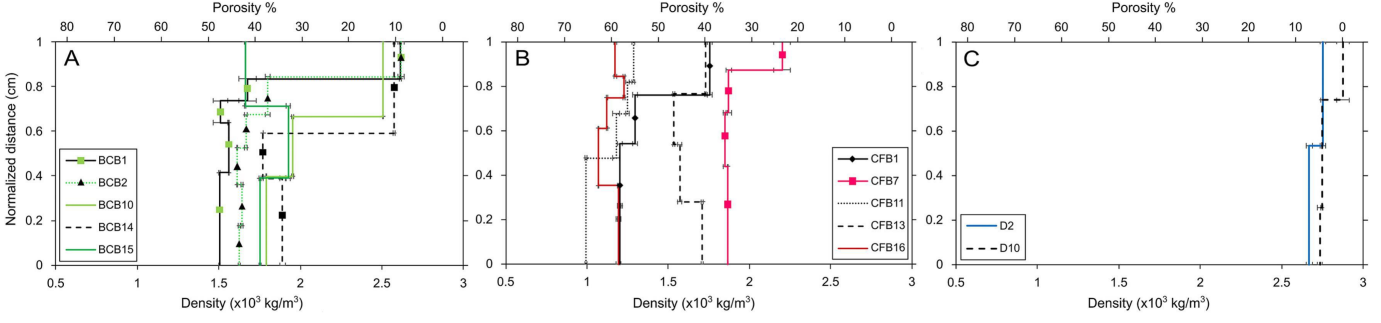
Porosity %
80 70 60 50 40 30 20 10 0
A
B
C
Normalized distance (cm)
0 0.2 0.4 0.6 0.8 1
BCB1
BCB2
BCB10
BCB14
BCB15
CFB1
CFB7
CFB11
CFB13
CFB16
D2
D10
0.5 1 1.5 2 2.5 3
Density (x10³ kg/m³)

Figure 5

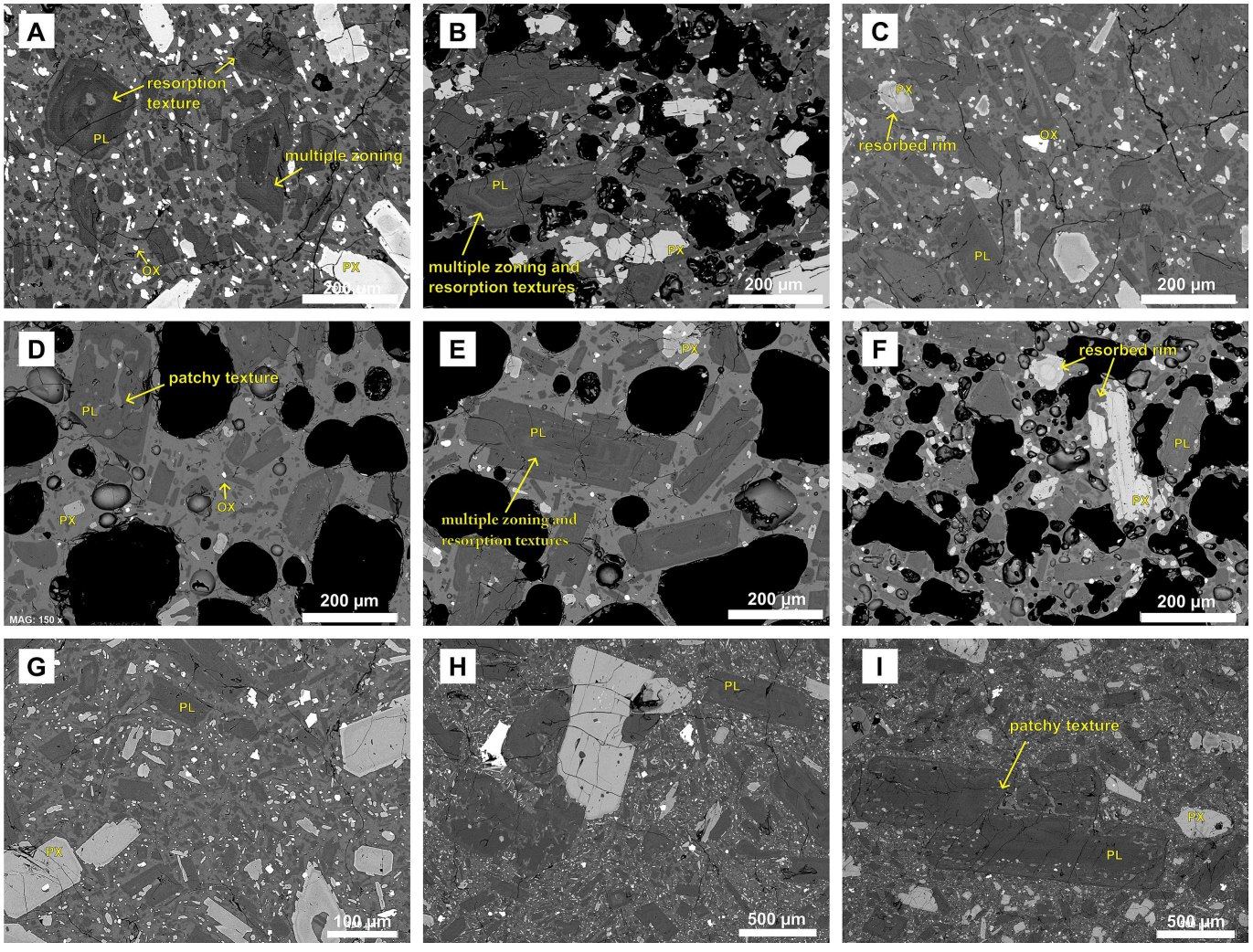
A
resorption texture
PL
multiple zoning
OX
PX
200 µm
B
PL
PX
multiple zoning and resorption textures
200 µm
C
PX
resorbed rim
OX
PL
200 µm
D
patchy texture
PL
OX
PX
200 µm
MAG: 150 x
E
PX
PL
multiple zoning and resorption textures
200 µm
F
resorbed rim
PL
PX
200 µm
G
PL
PX
100 µm
H
PL
500 µm
I
patchy texture
PX
PL
500 µm

Figure 6

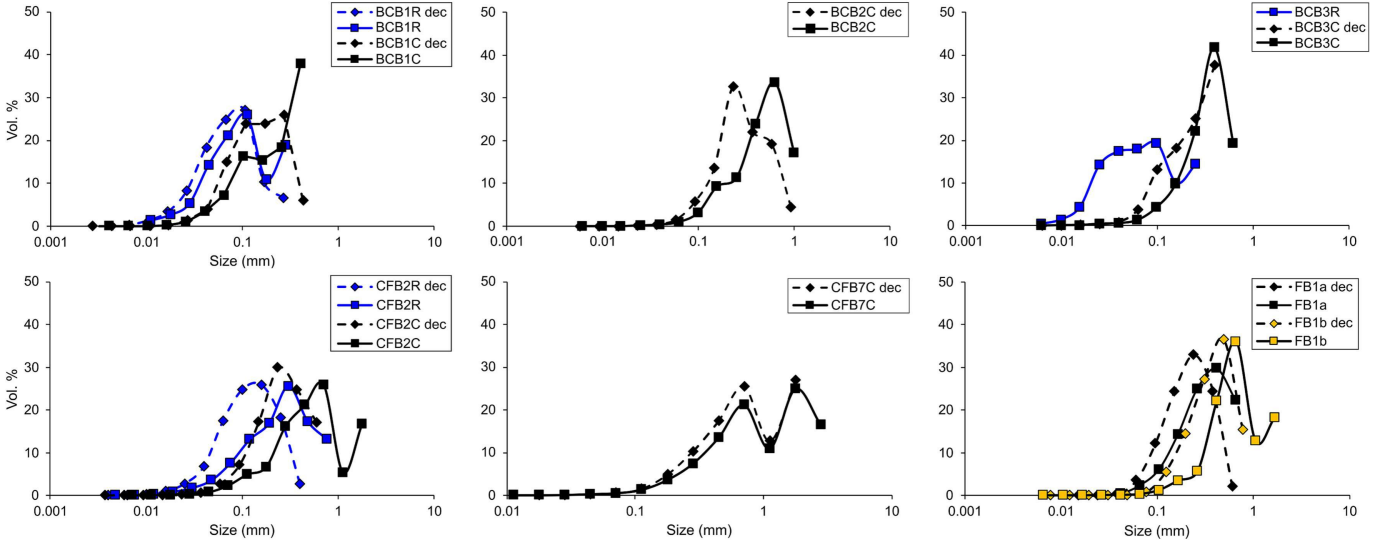
BCB1R dec
BCB1R
BCB1C dec
BCB1C
BCB2C dec
BCB2C
BCB3R
BCB3C dec
BCB3C
CFB2R dec
CFB2R
CFB2C dec
CFB2C
CFB7C dec
CFB7C
FB1a dec
FB1a
FB1b dec
FB1b
Vol. %
Size (mm)
0
10
20
30
40
50
0.001
0.01
0.1
1
10

Figure 7

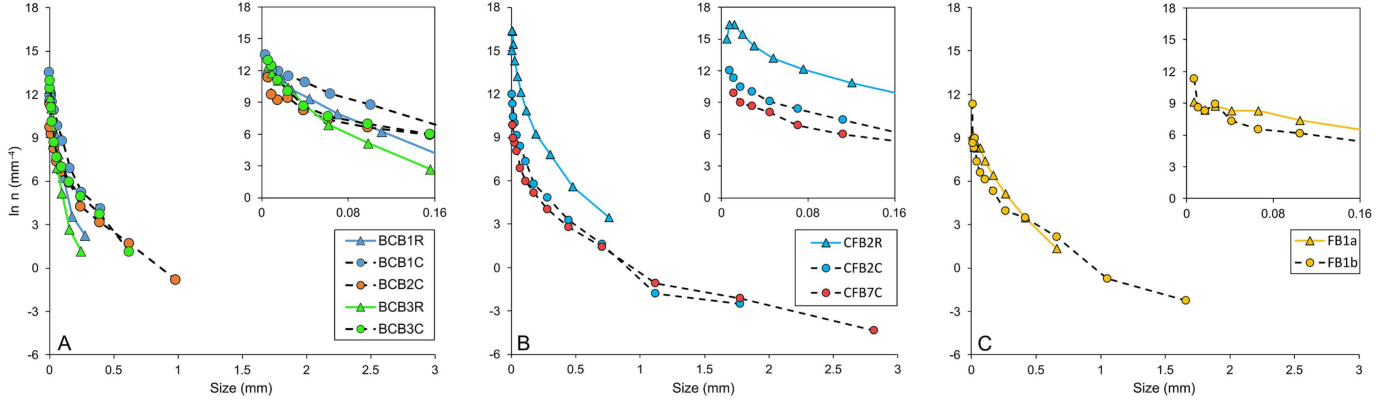
ln n (mm⁻⁴)
Size (mm)
A
BCB1R
BCB1C
BCB2C
BCB3R
BCB3C
B
CFB2R
CFB2C
CFB7C
C
FB1a
FB1b

Figure 8

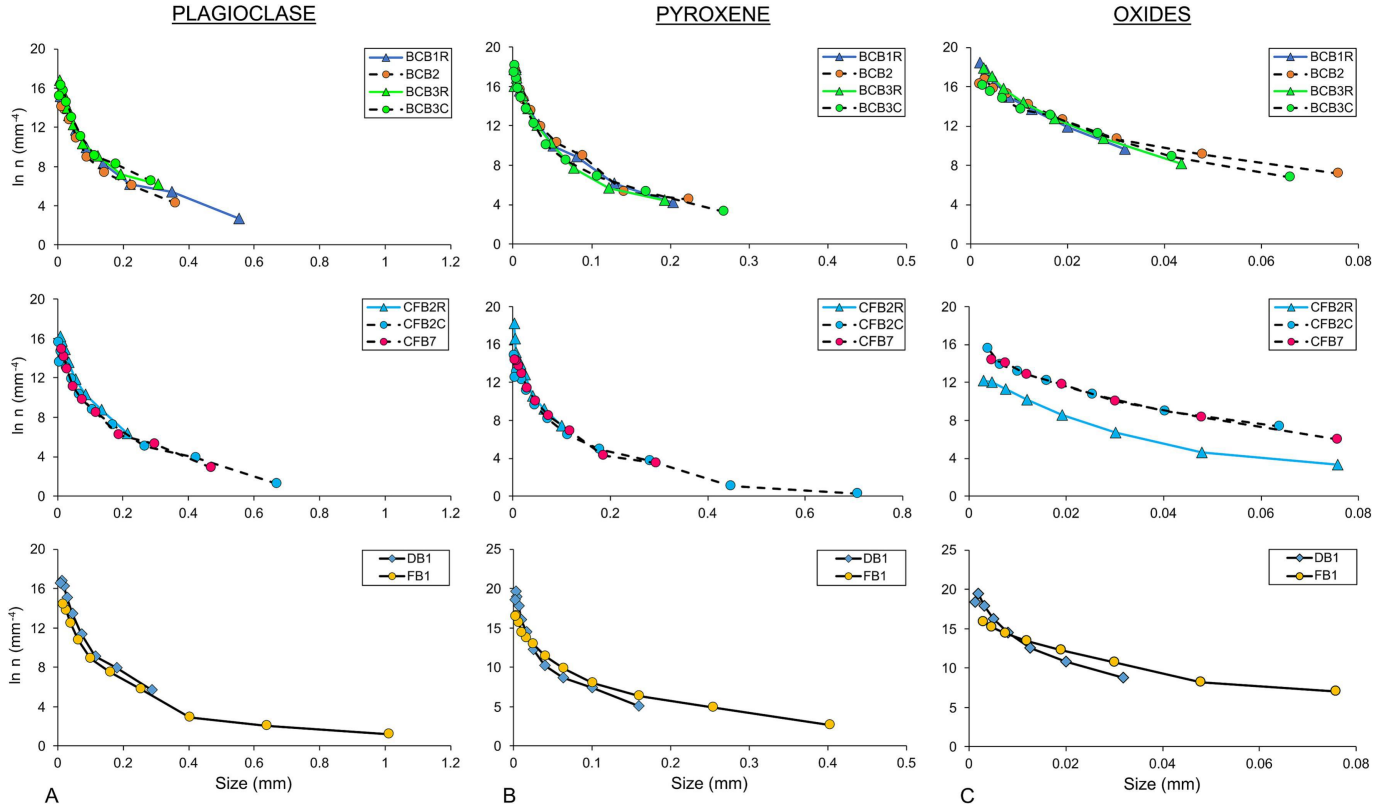
PLAGIOCLASE
PYROXENE
OXIDES
ln n (mm⁻⁴)
Size (mm)
BCB1R
BCB2
BCB3R
BCB3C
CFB2R
CFB2C
CFB7
DB1
FB1
A
B
C

Figure 9

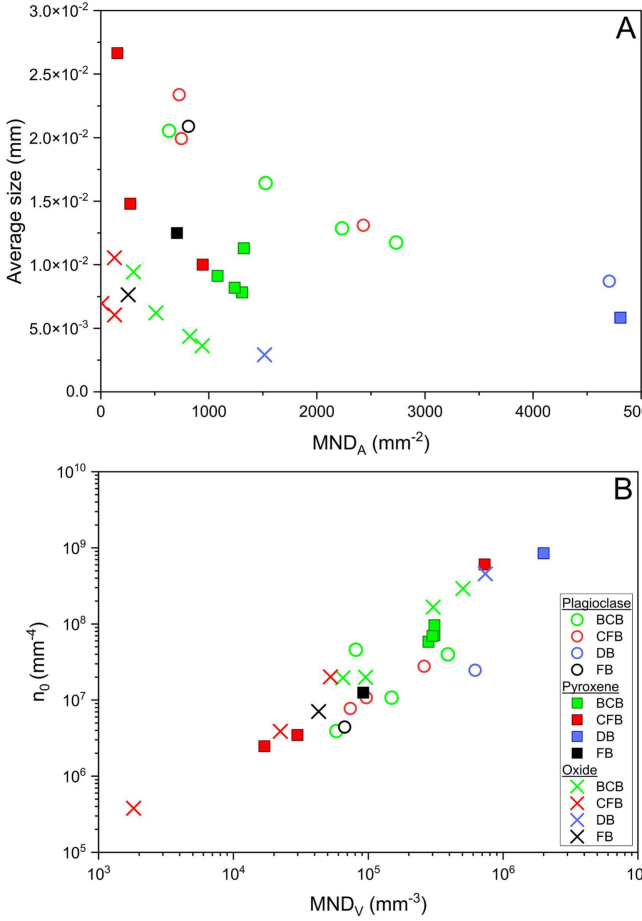
A
Average size (mm)
3.0×10-2
2.5×10-2
2.0×10-2
1.5×10-2
1.0×10-2
5.0×10-3
0.0
0
1000
2000
3000
4000
5000
MND_A (mm-2)
B
n0 (mm-4)
10^10
10^9
10^8
10^7
10^6
10^5
10^3
10^4
10^5
10^6
10^7
MND_V (mm-3)
Plagioclase
BCB
CFB
DB
FB
Pyroxene
BCB
CFB
DB
FB
Oxide
BCB
CFB
DB
FB

Figure 10

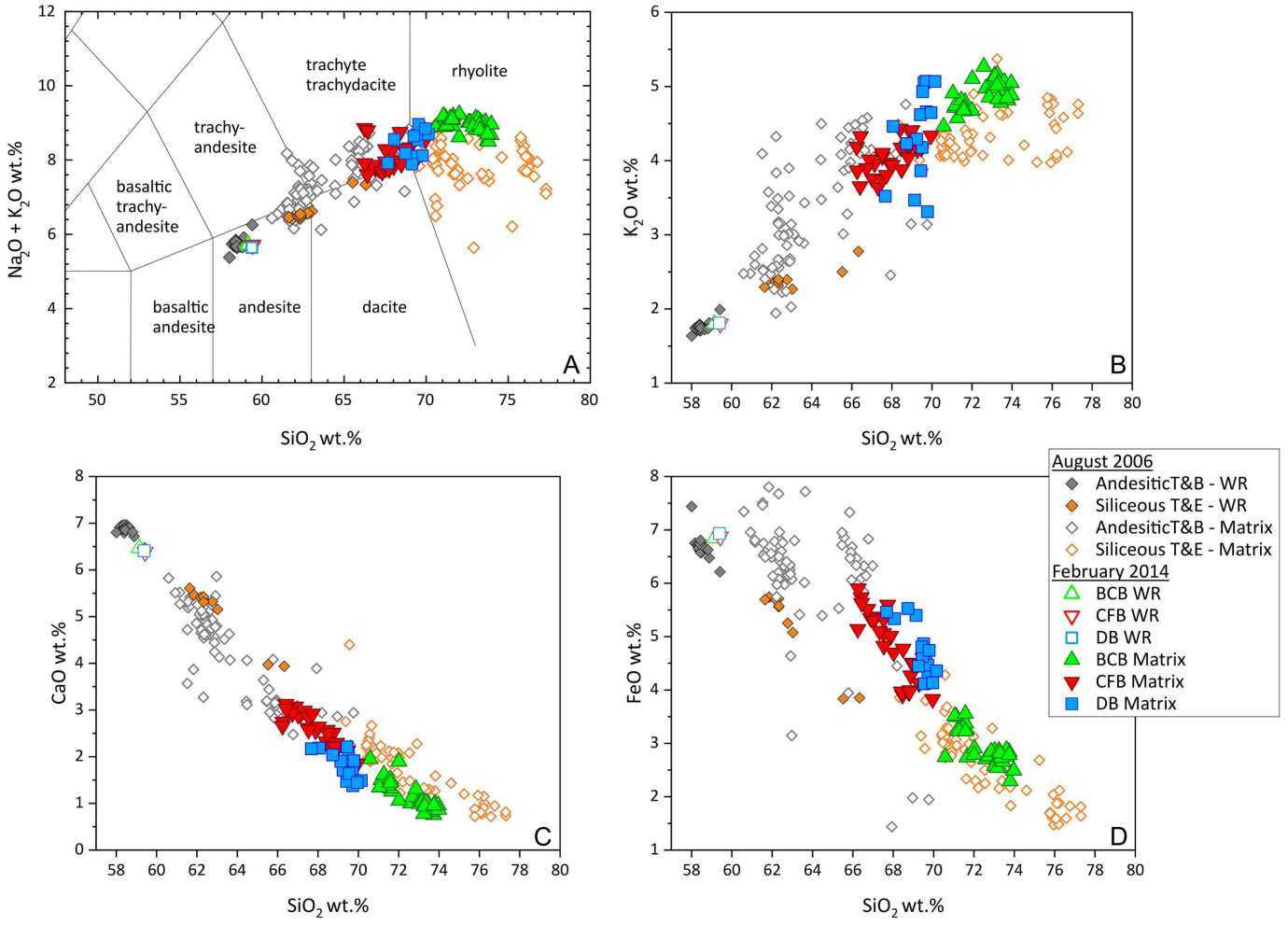
trachyte
trachydacite
rhyolite
trachy-
andesite
basaltic
trachy-
andesite
basaltic
andesite
andesite
dacite
A
$Na_2O + K_2O$ wt.%
SiO_2 wt.%
B
K_2O wt.%
SiO_2 wt.%
C
CaO wt.%
SiO_2 wt.%
D
FeO wt.%
SiO_2 wt.%
August 2006
AndesiticT&B - WR
Siliceous T&E - WR
AndesiticT&B - Matrix
Siliceous T&E - Matrix
February 2014
BCB WR
CFB WR
DB WR
BCB Matrix
CFB Matrix
DB Matrix

Figure 11

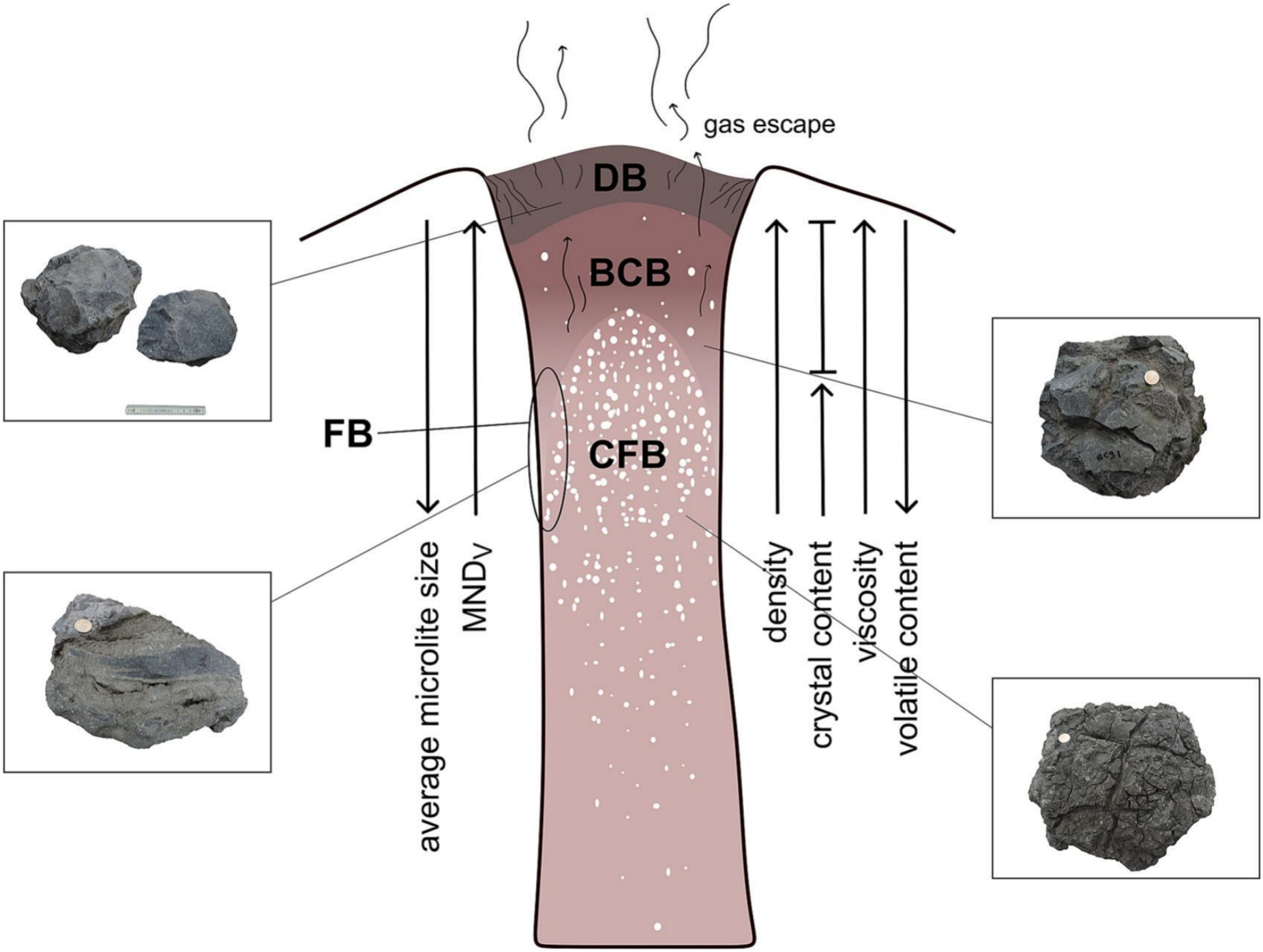
gas escape
DB
BCB
FB
CFB
average microlite size
MND$_V$
density
crystal content
viscosity
volatile content

Figure 12